Journal of Quantitative Spectroscopy & Radiative Transfer 111 (2010) 1025–1040

Contents lists available at ScienceDirect

Journal of Quantitative Spectroscopy & Radiative Transfer

journal homepage: www.elsevier.com/locate/jqsrt

A vector radiative transfer model for coupled atmosphere and ocean systems with a rough interface

Peng-Wang Zhai [a,*], Yongxiang Hu [b], Jacek Chowdhary [c], Charles R. Trepte [b], Patricia L. Lucker [a], Damien B. Josset [d]

[a] SSAI 1 Enterprise Parkway Suite 200, Hampton, VA 23666, USA
[b] MS 475 NASA Langley Research Center, Hampton, VA 23681-2199, USA
[c] Department of Applied Physics and Applied Mathematics, Columbia University, New York, NY, USA
[d] NASA Postdoctoral Program Fellow, NASA Langley Research Center, USA

ARTICLE INFO

Article history:
Received 16 October 2009
Received in revised form
8 December 2009
Accepted 9 December 2009

Keywords:
Atmospheric and ocean optics
Propagation
Transmission
Attenuation
Radiative transfer
Scattering
Polarization

ABSTRACT

We report on an exact vector (polarized) radiative transfer (VRT) model for coupled atmosphere and ocean systems. This VRT model is based on the successive order of scattering (SOS) method, which virtually takes all the multiple scattering processes into account, including atmospheric scattering, oceanic scattering, reflection and transmission through the rough ocean surface. The isotropic Cox–Munk wave model is used to derive the ref and transmission matrices for the rough ocean surface. Shadowing effects are included by the shadowing function. We validated the SOS results by comparing them with those calculated by two independent codes based on the doubling/adding and Monte Carlo methods. Two error analyses related to the ocean color remote sensing are performed in the coupled atmosphere and ocean systems. One is the scalar error caused by ignoring the polarization in the whole system. The other is the error introduced by ignoring the polarization of the light transmitted through the ocean interface. Both errors are significant for the cases studied. This code fits for the next generation of ocean color study because it converges fast for absorbing medium as, for instance, ocean.

1. Introduction

Radiative transfer theory [1–3] in a scattering medium is a sine qua non in the study of climate change. There are two essential parts to the climate change study. One is to observe and record the changes of the earth system. The other is to model the climate system numerically and find the dependence of the climate system on various components, such as aerosol, clouds, air–sea interaction, ocean productivity, etc. In the first part, one of the most important means is the satellite remote sensing, in which the radiative transfer theory is often used to interpret the satellite raw images to retrieve atmosphere or ocean components of interest [4,5]. In the second part, radiative transfer is used to calculate global and regional energy transfer and distribution in the earth system [5]. In other words, radiative transfer is indispensable in both parts.

Radiative transfer in the coupled atmosphere and ocean system (AOS) is particularly of interest because oceans occupy more than 70% of the earth surface area. Light reflection and refraction at the water interface need special treatment. For the sake of simplicity, many works assume the ocean surface to be flat [6–10], while ocean surfaces always have waves induced by wind and other factors in nature [11,12]. Many others ignore the polarization of light [13–17]. Using the scalar radiative transfer equation (ignoring the polarization) may introduce errors larger than 10% depending on the illuminating

* Corresponding author. Tel.: +1 757 951 1950.
E-mail address: Pengwang.zhai-1@nasa.gov (P.-W. Zhai).

0022-4073/$ - see front matter © 2009 Elsevier Ltd. All rights reserved.
doi:10.1016/j.jqsrt.2009.12.005

and viewing angles [18,19]. A short list of works that solve the polarized radiative transfer equation with a rough ocean surface are [20–25].

In this paper we present a vector (polarized) radiative transfer (VRT) model for the AOS under the plane-parallel assumption. The model is based on the successive order of scattering method (SOS) [8,9,26–37]. The full 4×4 reflection and transmission matrices for light interacting with the Gaussian rough surface are derived. The wave slope distribution is the isotropic Cox–Munk model (independent on the wind direction) [11,12]. Special routines have been designed to treat the singularities associated with the reflection and transmission matrices. Shadowing function has been implemented to take the shadowing effects into account [38–40]. A number of numerical techniques, for instance, the delta-fit for the phase matrix [9], the exponential-linear approximation for optical depth integration [41], and the geometric series approximation [31], have been implemented to increase efficiency while maintaining accuracy. In a nutshell, the SOS code can calculate the polarized light multiply scattered by the atmosphere, ocean, and rough ocean surface with all the coupling processes included. The doubling/adding code [22] and the Monte Carlo code [9,24] have been used for validation. We then used the SOS code to do two error analyses. One is the error introduced by neglecting the polarization in the whole system; and the other is the error caused by ignoring the polarization of light transmitted through the ocean interface.

The SOS method converges fast for absorbing or thin media. This makes it especially useful in the field of ocean color remote sensing because of two facts. One is that clear sky and low aerosol loading are the prerequisites for ocean color remote sensing; and the other is that oceans mostly exhibit large absorption coefficients. The notations and theoretical frame in this paper are the same as [9,28]. Section 2 reviews the integral form of the VRT equation. Section 3 shows the SOS formulas to solve the VRT equation with an emphasis to the boundary condition at the ocean interface. Sections 4–7 derive and discuss the reflection and transmission matrices at the ocean interface. Sections 8 and 9 are the verification and applications of the SOS code, respectively. The last section is the summary.

2. Integral form of the vector radiative transfer equation

The basic scenario is that the AOS is illuminated by the solar light source. The whole system is plane parallel, i.e., the inherent optical properties (IOP) only vary along one dimension. The radiance vector of a beam of light with arbitrary polarization is denoted as $\mathbf{L}=(I,Q,U,V)^T$, where the four elements I, Q, U, and V are the Stokes parameters (see [3], Eq. 2.6.4); the superscript T stands for transpose. The optical depth is denoted as τ and $\tau_l<\tau<\tau_u$, where the subscripts l and u denote the lower and upper limits of the medium under consideration (either the atmosphere or ocean). For the atmosphere, $\tau_l=0$ is at the top and $\tau_u=\tau_a^*$ at the bottom. For the ocean, $\tau_l=\tau_o$ is at the top and $\tau_u=\tau_o^*$ at the bottom. Note that τ_a^* is the location just above the ocean surface and $\tau_o=\tau_a^*+\varepsilon$ is just below the ocean surface, where ε is an infinitesimal.

The scattering matrix $\mathbf{F}(\tau,\Theta)$ is a function of τ and scattering angle Θ. The phase matrix is

$$\mathbf{P}(\tau,\mu,\phi,\mu',\phi')=\mathbf{R}(\pi-\chi_2)\cdot\mathbf{F}(\tau,\Theta)\cdot\mathbf{R}(-\chi_1), \tag{1}$$

where $\mathbf{R}$ is the rotation matrix which transforms the reference plane of the radiance vector between the meridian and scattering planes; χ_1 and χ_2 are the rotation angles [42,43]; $\mu=\cos(\theta)$ and ϕ are the cosine of the zenith angle and the azimuthal angle, respectively; the superscript prime denotes the incident direction; the cosine of the scattering angle can be written as $\cos(\Theta)=\mu\mu'+\sqrt{1-\mu^2}\sqrt{1-\mu'^2}\cos(\phi-\phi')$. The multiple scattering source matrix $\mathbf{S}$ in a macroscopically isotropic and mirror symmetric medium is [3]

$$\mathbf{S}(\tau,\mu,\phi)=\frac{\omega(\tau)}{4\pi}\int_0^{2\pi}\int_{-1}^{1}\mathbf{P}(\tau,\mu,\phi,\mu',\phi')\cdot\mathbf{L}(\tau,\mu',\phi')\,d\mu'\,d\phi', \tag{2}$$

where ω is the single scattering albedo.

When no thermal emission source is included, an integral form of the vector radiative transfer equation is written as [1,5,9]

$$\mathbf{L}(\tau,\mu<0,\phi)=\mathbf{L}(\tau_l,\mu,\phi)e^{-(\tau_l-\tau)/\mu}-\int_{\tau_l}^{\tau}e^{-(\tau'-\tau)/\mu}\mathbf{S}(\tau',\mu,\phi)\,d\tau'/\mu, \tag{3a}$$

$$\mathbf{L}(\tau,\mu>0,\phi)=\mathbf{L}(\tau_u,\mu,\phi)e^{-(\tau_u-\tau)/\mu}+\int_{\tau}^{\tau_u}e^{-(\tau'-\tau)/\mu}\mathbf{S}(\tau',\mu,\phi)\,d\tau'/\mu. \tag{3b}$$

3. Successive orders of scattering method

The total radiance vector can be treated as a summation of contributions from different order of scattering [26–28,30],

$$\mathbf{L}(\tau,\mu,\phi)=\sum_{n=1}^{N}\mathbf{L}_n(\tau,\mu,\phi). \tag{4}$$

With this equation, Eqs. (3a) and (3b) can be rearranged into

$$\mathbf{L}_n(\tau,\mu<0,\phi)=\mathbf{L}_n(\tau_l,\mu,\phi)e^{-(\tau_l-\tau)/\mu}-\int_{\tau_l}^{\tau}e^{-(\tau'-\tau)/\mu}\mathbf{S}_n(\tau',\mu,\phi)\,d\tau'/\mu, \tag{5a}$$

$$\mathbf{L}_n(\tau,\mu>0,\phi)=\mathbf{L}_n(\tau_u,\mu,\phi)e^{-(\tau_u-\tau)/\mu}+\int_{\tau}^{\tau_u}e^{-(\tau'-\tau)/\mu}\mathbf{S}_n(\tau',\mu,\phi)\,d\tau'/\mu, \tag{5b}$$

where

$$\mathbf{S}_n(\tau,\mu,\phi)=\frac{\omega(\tau)}{4\pi}\int_0^{2\pi}\int_{-1}^{1}\mathbf{P}(\tau,\mu,\phi,\mu',\phi')\cdot\mathbf{L}_{n-1}(\tau,\mu',\phi')\,d\mu'\,d\phi'. \tag{6}$$

A special case is for $n=1$ and $\tau<\tau_a^*$. In this case $\mathbf{L}_0(\tau<\tau_a^*,\mu',\phi')=\mathbf{E}_0e^{\tau/\mu_0}\delta(\mu'-\mu_0)\delta(\phi'-\phi_0)$, where $\mathbf{E}_0=(E_0,0,0,0)^T$ is the solar irradiance vector; $\mu_0=\cos(\theta_0)<0$

and ϕ_0 are the cosine of the solar zenith angle and the solar azimuthal angle, respectively; and δ is the Dirac delta function. After substituting $\mathbf{L}_0(\tau<\tau_a^*,\mu',\phi')$ into Eq. (6) and performing the integration, one obtains

$$\mathbf{S}_1(\tau<\tau_a^*,\mu,\phi)=\frac{\omega(\tau)}{4\pi}e^{\tau/\mu_0}\mathbf{P}(\tau,\mu,\phi,\mu_0,\phi_0)\cdot\mathbf{E}_0. \tag{7}$$

The radiance vectors at the boundaries are

$$\mathbf{L}_n(\tau=0,\mu<0,\phi)=0, \tag{8a}$$

$$\mathbf{L}_1(\tau_a^*,\mu>0,\phi)=|\mu_0|\mathbf{B}_r(\mu,\phi,\mu_0,\phi_0)\cdot\mathbf{E}_0e^{\tau_a^*/\mu_0}/\pi, \tag{8b}$$

$$\begin{aligned}\mathbf{L}_{n>1}(\tau_a^*,\mu>0,\phi)=&\frac{1}{\pi}\int_0^{2\pi}\int_{-1}^{0}\mathbf{B}_r(\mu,\phi,\mu',\phi')\\&\cdot\mathbf{L}_{n-1}(\tau_a^*,\mu',\phi')|\mu'|\,d\mu'\,d\phi'+\frac{1}{\pi}\int_0^{2\pi}\int_0^{1}\mathbf{B}_t'(\mu,\phi,\mu',\phi')\\&\cdot\mathbf{L}_{n-1}(\tau_o,\mu',\phi')|\mu'|\,d\mu'\,d\phi',\end{aligned} \tag{8c}$$

$$\mathbf{L}_1(\tau_o,\mu<0,\phi)=|\mu_0|\mathbf{B}_t(\mu,\phi,\mu_0,\phi_0)\cdot\mathbf{E}_0e^{\tau_a^*/\mu_0}/\pi, \tag{8d}$$

$$\begin{aligned}\mathbf{L}_{n>1}(\tau_o,\mu<0,\phi)=&\frac{1}{\pi}\int_0^{2\pi}\int_{-1}^{0}\mathbf{B}_t(\mu,\phi,\mu',\phi')\\&\cdot\mathbf{L}_{n-1}(\tau_a^*,\mu',\phi')|\mu'|\,d\mu'\,d\phi'+\frac{1}{\pi}\int_0^{2\pi}\int_0^{1}\mathbf{B}_r'(\mu,\phi,\mu',\phi')\\&\cdot\mathbf{L}_{n-1}(\tau_o,\mu',\phi')|\mu'|\,d\mu'\,d\phi',\end{aligned} \tag{8e}$$

$$\begin{aligned}\mathbf{L}_1(\tau_o^*,\mu>0,\phi)=&\int_0^{2\pi}\int_{-1}^{0}\frac{|\mu'|}{\pi}e^{(\tau_o^*-\tau_o)/\mu'}\mathbf{r}^*(\mu,\phi,\mu',\phi')\\&\cdot\mathbf{B}_t(\mu',\phi',\mu_0,\phi_0)\cdot\mathbf{E}_0\frac{|\mu_0|}{\pi}e^{\tau_a^*/\mu_0}\,d\mu'\,d\phi',\end{aligned} \tag{8f}$$

$$\begin{aligned}\mathbf{L}_{n>1}(\tau_o^*,\mu>0,\phi)=&\int_0^{2\pi}\int_{-1}^{0}\frac{|\mu'|}{\pi}\mathbf{r}^*(\mu,\phi,\mu',\phi')\\&\cdot\mathbf{L}_{n-1}(\tau_o^*,\mu',\phi')\,d\mu'\,d\phi',\end{aligned} \tag{8g}$$

where $\mathbf{r}^*$ is the reflection matrix of the ocean bottom; $\mathbf{B}_r$ and $\mathbf{B}_r'$ are the reflection matrices of the ocean interface for air and water incidence, respectively; and $\mathbf{B}_t$ and $\mathbf{B}_t'$ are the transmission matrices of the ocean interface for air and water incidence, respectively. Explicit expressions of these matrices related to a rough dielectric interface will be derived in Section 4. In Eqs. (8a)–(8g) and hereafter, $|\ldots|$ means the absolute value is taken. In the case of flat ocean interface, Eqs. (6)–(8) should be equivalent to Eqs. (7) and (8) in Ref. [9], though the arrangement is slightly different. In this paper, the first order source function in the atmosphere ($\mathbf{S}_1(\tau<\tau_a^*,\mu,\phi)$) only contains the contribution from the direct solar light; while in Ref. [9] $\mathbf{S}_1(\tau<\tau_a^*,\mu,\phi)$ also includes the contribution from the specular reflection of the direct solar light from the ocean interface. Similar differences exist for $\mathbf{S}_1(\tau>\tau_o,\mu,\phi)$. Correspondingly the boundary conditions for the radiance vectors also exhibit differences. As a whole, the total radiance field from the two sets of equations remains consistent.

Eqs. (4)–(8) represent a system of equations which can be solved with numerical iterative procedures. To reduce the computational cost, a common practice is to expand the azimuthal dependence of the VRT equation into the Fourier series. The radiance vectors can be expanded into

$$\begin{aligned}\mathbf{L}_n(\tau,\mu,\phi)=&\sum_{m=0}^{M}(2-\delta_{0m})\{\cos[m(\phi-\phi_0)]\mathbf{L}_{n,\cos}^m(\tau,\mu)\\&+\sin[m(\phi-\phi_0)]\mathbf{L}_{n,\sin}^m(\tau,\mu)\},\end{aligned} \tag{9}$$

with

$$\mathbf{L}_{n,\cos}^m(\tau,\mu)=(I_n^m,Q_n^m,0,0)^T, \tag{10a}$$

$$\mathbf{L}_{n,\sin}^m(\tau,\mu)=(0,0,U_n^m,V_n^m)^T. \tag{10b}$$

The expansion of the phase matrices is

$$\mathbf{P}(\tau,\mu,\phi,\mu',\phi')=\mathbf{P}_1(\tau,\mu,\phi,\mu',\phi')+\mathbf{P}_2(\tau,\mu,\phi,\mu',\phi'), \tag{11a}$$

$$\begin{aligned}\mathbf{P}_1(\tau,\mu,\phi,\mu',\phi')=&\begin{pmatrix}P_{11}&P_{12}&0&0\\P_{21}&P_{22}&0&0\\0&0&P_{33}&P_{34}\\0&0&P_{43}&P_{44}\end{pmatrix}\\=&\sum_{m=0}^{M}(2-\delta_{0m})\cos[m(\phi-\phi')]\mathbf{P}_{\cos}^m(\tau,\mu,\mu'),\end{aligned} \tag{11b}$$

$$\begin{aligned}\mathbf{P}_2(\tau,\mu,\phi,\mu',\phi')=&\begin{pmatrix}0&0&P_{13}&P_{14}\\0&0&P_{23}&P_{24}\\P_{31}&P_{32}&0&0\\P_{41}&P_{42}&0&0\end{pmatrix}\\=&\sum_{m=0}^{M}(2-\delta_{0m})\sin[m(\phi-\phi')]\mathbf{P}_{\sin}^m(\tau,\mu,\mu').\end{aligned} \tag{11c}$$

The detailed computation aspects of $\mathbf{P}_{\sin}^m$ and $\mathbf{P}_{\cos}^m$ can be found in [9] and the references within. Note that $\mathbf{B}_r$,$\mathbf{B}_r'$,$\mathbf{B}_t$,$\mathbf{B}_t'$, and $\mathbf{r}^*$ in Eqs. (8a) and (8g) can all be expanded into Fourier series in the same fashion as $\mathbf{P}$. These expansions will not be explicitly written out for conciseness. In the following, $\mathbf{B}_{r,\cos}^m$ and $\mathbf{B}_{r,\sin}^m$ will be the cosine and sine components for $\mathbf{B}_r$;$\mathbf{B}_{r,\cos}'^m$ and $\mathbf{B}_{r,\sin}'^m$ will be the cosine and sine components for $\mathbf{B}_r'$;$\mathbf{B}_{t,\cos}^m$ and $\mathbf{B}_{t,\sin}^m$ will be the cosine and sine components for $\mathbf{B}_t$;$\mathbf{B}_{t,\cos}'^m$ and $\mathbf{B}_{t,\sin}'^m$ will be the cosine and sine components for $\mathbf{B}_t'$; and $\mathbf{r}_{\cos}^{*,m}$ and $\mathbf{r}_{\sin}^{*,m}$ will be the cosine and sine components for $\mathbf{r}^*$. These expansions are then substituted into Eqs. (6) and (8). After carrying out the integration over ϕ' and identifying the terms with the same Fourier order m, the resultant formulas are (see [28,44–47] for details):

$$\mathbf{L}_n^m(\tau,\mu<0)=\mathbf{L}_n^m(\tau_l,\mu)e^{-(\tau_l-\tau)/\mu}-\int_{\tau_l}^{\tau}e^{-(\tau'-\tau)/\mu}\mathbf{S}_n^m(\tau',\mu)\,d\tau'/\mu, \tag{12a}$$

$$\mathbf{L}_n^m(\tau,\mu>0)=\mathbf{L}_n^m(\tau_u,\mu)e^{-(\tau_u-\tau)/\mu}+\int_{\tau}^{\tau_u}e^{-(\tau'-\tau)/\mu}\mathbf{S}_n^m(\tau',\mu)\,d\tau'/\mu, \tag{12b}$$

where

$$\mathbf{S}_n^m(\tau,\mu)=\frac{\omega(\tau)}{2}\int_{-1}^{1}\mathbf{P}^m(\tau,\mu,\mu')\mathbf{L}_{n-1}^m(\tau,\mu')\,d\mu', \tag{13}$$

with the special case of

$$\mathbf{S}_1^m(\tau<\tau_a^*,\mu)=\frac{\omega(\tau)}{4\pi}e^{\tau/\mu_0}\mathbf{P}^m(\tau,\mu,\mu_0)\mathbf{E}_0, \tag{14}$$

where $\mathbf{L}_n^m = \mathbf{L}_{n,\cos}^m + \mathbf{L}_{n,\sin}^m$ and $\mathbf{P}^m = \mathbf{P}_{\cos}^m + \mathbf{P}_{\sin}^m \cdot \mathbf{D}$ with $\mathbf{D} = \mathrm{diag}\{1, 1, -1, -1\}$ [28]; and

$$\mathbf{L}_n^m(\tau = 0, \mu < 0) = 0, \tag{15a}$$

$$\mathbf{L}_1^m(\tau_a^*, \mu > 0) = |\mu_0| \mathbf{B}_r^m(\mu, \mu_0) \cdot \mathbf{E}_0 e^{\tau_a^*/\mu_0}/\pi, \tag{15b}$$

$$\mathbf{L}_{n>1}^m(\tau_a^*, \mu > 0) = 2\int_{-1}^{0} \mathbf{B}_r^m(\mu, \mu') \cdot \mathbf{L}_{n-1}^m(\tau_a^*, \mu')|\mu'|\, d\mu' + 2\int_0^1 \mathbf{B}_t^{'m}(\mu, \mu') \cdot \mathbf{L}_{n-1}^m(\tau_o, \mu')|\mu'|\, d\mu', \tag{15c}$$

$$\mathbf{L}_1^m(\tau_o, \mu < 0) = |\mu_0| \mathbf{B}_t^m(\mu, \mu_0) \cdot \mathbf{E}_0 e^{\tau_a^*/\mu_0}/\pi, \tag{15d}$$

$$\mathbf{L}_{n>1}^m(\tau_o, \mu < 0) = 2\int_{-1}^{0} \mathbf{B}_t^m(\mu, \mu') \cdot \mathbf{L}_{n-1}^m(\tau_a^*, \mu')|\mu'|\, d\mu' + 2\int_0^1 \mathbf{B}_r^{'m}(\mu, \mu') \cdot \mathbf{L}_{n-1}^m(\tau_o, \mu',)|\mu'|\, d\mu', \tag{15e}$$

$$\mathbf{L}_1^m(\tau_o^*, \mu > 0) = 2\int_{-1}^{0} \frac{|\mu'|}{\pi} e^{(\tau_o^* - \tau_o)/\mu'} \mathbf{r}^*(\mu, \mu') \cdot \mathbf{B}_t^m(\mu', \mu_0) \cdot \mathbf{E}_0 |\mu_0| e^{\tau_a^*/\mu_0}\, d\mu', \tag{15f}$$

$$\mathbf{L}_{n>1}^m(\tau_o^*, \mu > 0) = 2\int_{-1}^{0} |\mu'| \mathbf{r}^{*m}(\mu, \mu') \cdot \mathbf{L}_{n-1}^m(\tau_o^*, \mu')\, d\mu', \tag{15g}$$

where $\mathbf{r}^{*m}$, $\mathbf{B}_r^m$, $\mathbf{B}_r^{'m}$, $\mathbf{B}_t^m$, and $\mathbf{B}_t^{'m}$ follow the same notations as $\mathbf{P}^m$, i.e., $\mathbf{r}^{*m} = \mathbf{r}_{\cos}^{*m} + \mathbf{r}_{\sin}^{*m} \cdot \mathbf{D}$; $\mathbf{B}_r^m = \mathbf{B}_{r,\cos}^m + \mathbf{B}_{r,\sin}^m \cdot \mathbf{D}$; $\mathbf{B}_r^{'m} = \mathbf{B}_{r,\cos}^{'m} + \mathbf{B}_{r,\sin}^{'m} \cdot \mathbf{D}$; $\mathbf{B}_t^m = \mathbf{B}_{t,\cos}^m + \mathbf{B}_{t,\sin}^m \cdot \mathbf{D}$; and $\mathbf{B}_t^{'m} = \mathbf{B}_{t,\cos}^{'m} + \mathbf{B}_{t,\sin}^{'m} \cdot \mathbf{D}$.

4. The reflection matrix of a wind ruffled water surface

In this section, we will derive the reflection matrix for the wind ruffled water surface. Following Cox and Munk [11,12], we approximate the ocean surface by a distribution of small facets with random orientation. Note that this work ignores the wind-directionality of the facet distribution. As shown in Fig. 1, Σ and $d\Sigma$ are used to denote a small horizontal area of water surface and its fraction whose normal vector (μ_n, ϕ_n) is within a small solid angle of $d\omega_n$, respectively. In the previous statement, $\mu_n = \cos(\theta_n)$ where $\theta_n < \pi/2$ and ϕ_n are the polar and azimuthal angles of the surface normal vector, respectively. Σ and $d\Sigma$ satisfy the following relation [28]:

$$d\Sigma/\Sigma = p(\mu_n, \phi_n)\, d\omega_n, \tag{16}$$

where $p(\mu_n, \phi_n)$ is the probability distribution function. We will use the isotropic Cox–Munk model [11,12]:

$$p(\mu_n, \phi_n) = \frac{1}{\pi\sigma^2\mu_n^3} \exp\left(-\frac{1-\mu_n^2}{\sigma^2\mu_n^2}\right), \tag{17}$$

where the variance σ^2 is a function of the wind speed W(m/s) at 12 m above the ocean surface:

$$\sigma^2 = 0.003 + 0.00512W. \tag{18}$$

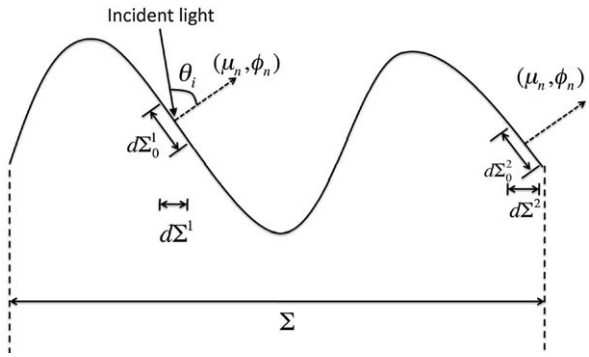

Fig. 1. A 2-D sketch of the ocean surface. $d\Sigma = d\Sigma^1 + d\Sigma^2 + \cdots + d\Sigma^j + \cdots$; $d\Sigma_0 = d\Sigma_0^1 + d\Sigma_0^2 + \cdots + d\Sigma_0^j + \cdots$; and $d\Sigma_0 = d\Sigma/\mu_n$. The superscript j in this figure is used to label the small fractions of the ocean surface whose normals are within a solid angle element of $d\omega_n$. $j =$ 1 and 2 are shown in the figure. θ_i is the angle of incidence.

Consider this small area Σ is illuminated by a beam of unpolarized light with irradiance E' from direction (μ', ϕ'). This beam is then reflected into direction (μ, ϕ) within a solid angle of $d\omega$. The power of specular reflection is then $r(\theta_i)d\Sigma_0\cos(\theta_i)E'$, where $r(\theta_i)$ is the Fresnel's reflection coefficient; θ_i is the angle of incidence on the surface elements; and $d\Sigma_0$ is the effective surface area which reflects the incident light from (μ', ϕ') to (μ, ϕ), i.e., $d\Sigma_0 = d\Sigma/\mu_n$. Also the reflected power is $|\mu| L_r \Sigma d\omega$, where L_r is the reflected radiance. Indeed, these two powers are equal because they represent the same quantity:

$$|\mu| L_r \Sigma d\omega = r(\theta_i) d\Sigma_0 \cos(\theta_i) E', \tag{19}$$

which leads to

$$L_r = \frac{r(\theta_i)p(\mu_n, \phi_n)E'}{|\mu|\mu_n} \frac{d\omega_n \cos(\theta_i)}{d\omega} = \frac{r(\theta_i)p(\mu_n, \phi_n)E'}{4|\mu|\mu_n}, \tag{20}$$

where $d\omega_n = \sin(\theta_i)\, d\theta_i\, d\psi$, $d\omega = \sin(2\theta_i) d(2\theta_i) d\psi$, and Eq. (16) have been used. The quantity $d\theta_i$ is the variance of the angle of incidence; and $d\psi$ is defined as the angle variance perpendicular to $d\theta_i$. Furthermore, the shadowing effects should be considered because some of the surface elements will be blocked by other elements if viewing from the propagation direction of light. It is taken into account by multiplying Eq. (20) with the shadowing function [38,39]:

$$S(\mu, \mu') = \frac{1}{1 + \Lambda(\mu) + \Lambda(\mu')}, \tag{21}$$

where

$$\Lambda(\mu) = \frac{1}{2}\left\{\frac{1}{\sqrt{\pi}}\frac{1}{\eta}\exp(-\eta^2) - \mathrm{erfc}(\eta)\right\}; \tag{22}$$

η is defined as

$$\eta = \frac{\mu}{\sigma\sqrt{1-\mu^2}}; \tag{23}$$

erfc is the complementary error function [48]; and σ is the same as in Eq. (18). The reflection function B_r is then

$$|\mu'| B_r(\theta_i) = S(\mu, \mu') \frac{\pi p(\mu_n, \phi_n)}{4|\mu|\mu_n} r(\theta_i). \tag{24}$$

Note that Eq. (24) is equivalent to the results in [13,40].

The generalization of Eq. (24) to the case with polarization is fairly straightforward. First the reflection coefficient $r(\theta_i)$ will be replaced by the reflection matrix $\mathbf{r}$ (see Section 6 for explicit expressions). Then the rotations of the radiance vectors between the meridian and scattering planes have to be taken into account. The result is

$$|\mu'|\mathbf{B}_r(\theta_i) = S(\mu,\mu')\frac{\pi p(\mu_n,\phi_n)}{4|\mu|\mu_n}\mathbf{R}(\pi-\chi_2)\cdot\mathbf{r}(\theta_i)\cdot\mathbf{R}(-\chi_1). \quad (25)$$

Eq. (25) can be written as a function of (μ,ϕ) and (μ',ϕ') explicitly. For convenience, $\hat{\mathbf{n}}'$, $\hat{\mathbf{n}}$, and $\hat{\mathbf{n}}_n$ will be used for the unit vectors of incidence, reflection, and wave normal, respectively:

$$\hat{\mathbf{n}}' = (\sqrt{1-\mu'^2}\cos(\phi'), \sqrt{1-\mu'^2}\sin(\phi'), \mu'), \quad (26a)$$

$$\hat{\mathbf{n}} = (\sqrt{1-\mu^2}\cos(\phi), \sqrt{1-\mu^2}\sin(\phi), \mu), \quad (26b)$$

$$\hat{\mathbf{n}}_n = (\sqrt{1-\mu_n^2}\cos(\phi_n), \sqrt{1-\mu_n^2}\sin(\phi_n), \mu_n). \quad (26c)$$

For the air-incident case, the relation among the three vectors is (see Fig. 4.2 in [16]):

$$\hat{\mathbf{n}}_n = \frac{\hat{\mathbf{n}}-\hat{\mathbf{n}}'}{|\hat{\mathbf{n}}-\hat{\mathbf{n}}'|}, \quad (27)$$

where $|\hat{\mathbf{n}}-\hat{\mathbf{n}}'| = \sqrt{2-2\cos(\Theta)}$ and $\cos(\Theta) = \mu\mu' + \sqrt{1-\mu'^2}\sqrt{1-\mu^2}\cos(\phi-\phi')$ is the cosine of the scattering angle. Therefore, we have

$$\mu_n = \frac{\mu-\mu'}{\sqrt{2-2\cos(\Theta)}}. \quad (28)$$

Also, the angle of incidence θ_i is related to the scattering angle Θ by $\theta_i = (\pi-\Theta)/2$. Substituting Eqs. (17) and (28) into Eq. (25) leads to

$$|\mu'|\mathbf{B}_r = h_r(\mu,\phi,\mu',\phi')\mathbf{F}_r(\Theta), \quad (29a)$$

$$\mathbf{F}_r(\Theta) = (1-\cos(\Theta))^2\mathbf{R}(\pi-\chi_2)\cdot\mathbf{r}((\pi-\Theta)/2)\cdot\mathbf{R}(-\chi_1), \quad (29b)$$

$$h_r(\mu,\phi,\mu',\phi') = A_r\exp(-a_r)\exp(b_r\cos(\phi-\phi')), \quad (29c)$$

$$A_r = \frac{S(\mu,\mu')}{\sigma^2|\mu|(\mu-\mu')^4}, \quad (29d)$$

$$a_r = \frac{2-\mu^2-\mu'^2}{\sigma^2(\mu-\mu')^2}, \quad (29e)$$

$$b_r = \frac{2\sqrt{1-\mu'^2}\sqrt{1-\mu^2}}{\sigma^2(\mu-\mu')^2}. \quad (29f)$$

The reflection matrix $\mathbf{B}_r$ has been written into two parts. One is the scalar function h_r, which depends on both (μ',ϕ') and (μ,ϕ). The other is the matrix $\mathbf{F}_r$ which only depends on the scattering angle Θ. This arrangement was chosen in order to use the method by Deuzé et al. [45] to obtain the Fourier series of the reflection matrix. It can be shown that Eqs. (29a)–(29b) also apply to the water-incident case.

5. The transmission matrix of wind ruffled water surface

The derivation of the transmission matrix is similar to that of the reflection matrix. Consider the same scenario as the reflection case, with the exception that the outgoing radiance Eq. (19) is now considered as the transmitted radiance. The reflection coefficients $r(\theta_i)$ should be replaced by the transmission coefficients $t(\theta_i) = 1-r(\theta_i)$. After little rearrangement, the transmitted radiance due to the incident beam is now:

$$L_t = S(\mu,\mu')\frac{t(\theta_i)p(\mu_n,\phi_n)E'}{|\mu|\mu_n}\frac{d\omega_n\cos(\theta_i)}{d\omega}. \quad (30)$$

If $d\omega_n = \sin(\theta_i)\,d\theta_i\,d\psi$, then $d\omega = \sin(\theta_i-\theta_t)\,d(\theta_i-\theta_t)\,d\psi$, where θ_t is the angle of transmission (refraction) given by Snell's law $n_i\sin(\theta_i) = n_t\sin(\theta_t)$, with n_i and n_t refractive indices of the incident and transmitted media, respectively. The relation $n_t\cos(\theta_t)\,d\theta_t = n_i\cos(\theta_i)\,d\theta_i$ is obtained by taking a derivative of Snell's law. The ratio of the two solid angles is then:

$$\frac{d\omega_n}{d\omega} = \frac{\sin(\theta_i)\,d\theta_i\,d\psi}{(\sin(\theta_i)\cos(\theta_t)-\cos(\theta_i)\sin(\theta_t))(1-n_i\cos(\theta_i)/n_t\cos(\theta_t))\,d\theta_i\,d\psi}$$
$$= \frac{n_t^2\cos(\theta_t)}{(n_t\cos(\theta_t)-n_i\cos(\theta_i))^2}. \quad (31)$$

The following equation is obtained by substituting Eq. (31) into Eq. (30):

$$L_t = S(\mu,\mu')\frac{t(\theta_i)p(\mu_n,\phi_n)E'}{|\mu|\mu_n}\frac{n_t^2\cos(\theta_t)\cos(\theta_i)}{(n_t\cos(\theta_t)-n_i\cos(\theta_i))^2}. \quad (32)$$

Finally, the transmission function is

$$|\mu'|B_t = S(\mu,\mu')\frac{\pi t(\theta_i)p(\mu_n,\phi_n)}{|\mu|\mu_n}\frac{n_t^2\cos(\theta_t)\cos(\theta_i)}{(n_t\cos(\theta_t)-n_i\cos(\theta_i))^2}. \quad (33)$$

Eq. (33) can be extended to include the polarization using the similar consideration made for the reflection matrix:

$$|\mu'|\mathbf{B}_t = S(\mu,\mu')\frac{\pi p(\mu_n,\phi_n)}{|\mu|\mu_n}\frac{n_t^2\cos(\theta_t)\cos(\theta_i)}{(n_t\cos(\theta_t)-n_i\cos(\theta_i))^2}\mathbf{R}(\pi-\chi_2)$$
$$\cdot\,\mathbf{t}(\theta_i)\cdot\mathbf{R}(-\chi_1). \quad (34)$$

To express $|\mu'|\mathbf{B}_t$ as a function of (μ',ϕ') and (μ,ϕ), one has to write (μ_n,ϕ_n), $\cos(\theta_i)$, and $\cos(\theta_t)$ in terms of these quantities. First, we consider the air-incident case. In the derivation of $\mathbf{B}_t$, $\hat{\mathbf{n}}$ will be understood as the unit vector along the transmitted direction. This is consistent with the definition of $\hat{\mathbf{n}}$ in the reflection matrix because in both cases $\hat{\mathbf{n}}$ represents the direction of the exit (reflected/ transmitted) radiance. Again, $\hat{\mathbf{n}}'$ and $\hat{\mathbf{n}}_n$ are still the incident and surface normal vectors, respectively. The relation among these three vectors is (see Fig. 4.2 in [16])

$$\hat{\mathbf{n}}_n = \frac{\hat{\mathbf{n}}'-n_w\hat{\mathbf{n}}}{C}, \quad (35)$$

where n_w is the refractive index of water, and C is a normalization factor:

$$C = \frac{\sin(\Theta)}{\sin(\theta_i)}n_w = \frac{\sin(\Theta)}{\sin(\theta_t)}, \quad (36)$$

where $\Theta=\theta_i-\theta_t$ is the scattering angle. $1/n_w \le \cos(\Theta) \le 1$ has to be satisfied. The following equations are then obtained:

$$\cos(\theta_i) = -\hat{\mathbf{n}}_n \cdot \hat{\mathbf{n}}' = \frac{n_w\cos(\Theta)-1}{C}, \tag{37a}$$

$$\cos(\theta_t) = -\hat{\mathbf{n}}_n \cdot \hat{\mathbf{n}} = \frac{n_w-\cos(\Theta)}{C}. \tag{37b}$$

Another form for C can be obtained by substituting Eq. (36) into Eq. (37b):

$$C^2 = n_w^2+1-2n_w\cos(\Theta). \tag{38}$$

The component of $\hat{\mathbf{n}}_n$ (Eq. (35)) along the vertical direction z gives μ_n:

$$\mu_n = \frac{\mu'-n_w\mu}{C}. \tag{39}$$

The transmission matrix is obtained by the use of Eqs. (36)–(39):

$$|\mu'|\mathbf{B}_t = h_t(\mu,\phi,\mu',\phi')\mathbf{F}_t(\Theta), \tag{40a}$$

$$\mathbf{F}_t(\Theta) = (n_w-\cos(\Theta))(n_w\cos(\Theta)-1)\mathbf{R}(\pi-\chi_2)\cdot\mathbf{t}(\theta_i) \cdot \mathbf{R}(-\chi_1), \tag{40b}$$

$$h_t(\mu,\phi,\mu',\phi') = A_t\exp(-a_t)\exp(b_t\cos(\phi-\phi')), \tag{40c}$$

$$A_t = \frac{S(\mu,\mu')n_w^2}{\sigma^2|\mu|(\mu'-n_w\mu)^4}, \tag{40d}$$

$$a_t = \frac{1-\mu'^2+n_w^2(1-\mu^2)}{\sigma^2(\mu'-n_w\mu)^2}, \tag{40e}$$

$$b_t = \frac{2n_w\sqrt{1-\mu'^2}\sqrt{1-\mu^2}}{\sigma^2(\mu'-n_w\mu)^2}. \tag{40f}$$

For the water-incident case, one has

$$\hat{\mathbf{n}}_n = \frac{n_w\hat{\mathbf{n}}'-\hat{\mathbf{n}}}{C}, \tag{41}$$

with C given by Eq. (38) (Eq. (36), however, does not apply to the water-incident case). Following the same procedure, one find that the result is similar to Eqs. (40) except that new definitions of A_t, a_t, and b_t are needed:

$$|\mu'|\mathbf{B}'_t = h'_t(\mu,\phi,\mu',\phi')\mathbf{F}_t(\Theta), \tag{42a}$$

$$\mathbf{F}'_t(\Theta) = (n_w-\cos(\Theta))(n_w\cos(\Theta)-1)\mathbf{R}(\pi-\chi_2)\cdot\mathbf{t}(\theta_i) \cdot \mathbf{R}(-\chi_1), \tag{42b}$$

$$h'_t(\mu,\phi,\mu',\phi') = A'_t\exp(-a'_t)\exp(b'_t\cos(\phi-\phi')), \tag{42c}$$

$$A'_t = \frac{S(\mu,\mu')}{\sigma^2|\mu|(n_w\mu'-\mu)^4}, \tag{42d}$$

$$a'_t = \frac{n_w^2(1-\mu'^2)+(1-\mu^2)}{\sigma^2(n_w\mu'-\mu)^2}, \tag{42e}$$

$$b'_t = \frac{2n_w\sqrt{1-\mu'^2}\sqrt{1-\mu^2}}{\sigma^2(n_w\mu'-\mu)^2} \tag{42f}$$

For a beam of light incident onto a wind ruffled ocean surface, the incident irradiance has to be equal to the sum of the total reflected and transmitted irradiance, due to the law of energy conservation. To measure the degree of energy conservation of these formulas, Nakajima and Tanaka have defined the energy deficiency $\xi(\mu')$ [13]:

$$\xi(\mu') = 1-\frac{R(\mu')}{|\mu'|}-\frac{T(\mu')}{|\mu'|}, \tag{43}$$

where

$$R(\mu') = \frac{1}{\pi}\int_0^1 \mu d\mu \int_0^{2\pi} d\phi|\mu'|\mathbf{B}_r(\mu,\mu',\phi-\phi'), \tag{44a}$$

$$T(\mu') = \frac{1}{\pi}\int_{-1}^0 |\mu| d\mu \int_0^{2\pi} d\phi|\mu'|\mathbf{B}_t(\mu,\mu',\phi-\phi'). \tag{44b}$$

Ideally, ξ should be zero for every value of μ'. However, it has been shown that $\xi(\mu')$ has values as large as 0.15 for large angles of incidence (small $|\mu'|$) [13,22]. This energy deficiency $\xi(\mu')$ is commonly explained as a result of neglecting multiple scattering between the random wave facets [13,22]. To preserve energy conservation, Nakajima and Tanaka [13] divide Eqs. (25) and (34) by the energy deficiency ξ to normalize the reflectance and transmittance. Chowdhary [22] prefers to normalize the same equations according to the reflectance and transmittance of a smooth ocean surface. However, radiative transfer codes for atmospheres bounded by a rough ocean surface (i.e., no ocean medium is considered) generally do not account for this problem at all [28,40]. The ultimate answer to the renormalization problem relies on further improvements in the description of the shadowing function and accurate comparisons between theory and in situ measurements. In this work we avoid normalizing Eqs. (25) and (34) to simplify the comparison of our numerical results with those obtained by other radiative transfer codes.

6. Fresnel's reflection and transmission matrices

The Fresnel's reflection and transmission matrices $\mathbf{r}(\theta_i)$ and $\mathbf{t}(\theta_i)$ for a flat dielectric interface in Eqs. (25) and (34) have been presented in a few papers [8,20,21]. The matrices in [20] are for a different convention of the Stokes parameters, while [8] shows only the upper and left 3×3 sub-matrices of $\mathbf{r}(\theta_i)$ and $\mathbf{t}(\theta_i)$. The transmission matrix in [21] differs from the matrix used in this work for a coefficient. To avoid potential confusion caused by these differences, explicit expressions of $\mathbf{r}(\theta_i)$ and $\mathbf{t}(\theta_i)$ are derived and shown in this section.

A plane wave is incident from medium 1 with the index of refraction n_i. It is transmitted into medium 2 with the index of refraction n_t. In the case of incidence from air to water, $n_i=1$ and $n_t=n_w$. The permeabilities for both media are equal to 1 in the following equations. The plane of incidence (which is also the plane of scattering) is defined as the plane which contains the wave vectors of the incident, reflected, and transmitted waves. The relative amplitudes of the reflected and transmitted waves can be found with the boundary conditions for electromagnetic waves across the dielectric interface: (see

Eqs. 7.39 and 7.41 in [49]):

$$r_\perp = \frac{n_i\cos(\theta_i) - \sqrt{n_t^2 - n_i^2\sin^2(\theta_i)}}{n_i\cos(\theta_i) + \sqrt{n_t^2 - n_i^2\sin^2(\theta_i)}},$$

$$r_\parallel = \frac{n_t^2\cos(\theta_i) - n_i\sqrt{n_t^2 - n_i^2\sin^2(\theta_i)}}{n_t^2\cos(\theta_i) + n_i\sqrt{n_t^2 - n_i^2\sin^2(\theta_i)}}, \tag{45}$$

$$t_\perp = \frac{2n_i\cos(\theta_i)}{n_i\cos(\theta_i) + \sqrt{n_t^2 - n_i^2\sin^2(\theta_i)}},$$

$$t_\parallel = \frac{2n_i n_t\cos(\theta_i)}{n_t^2\cos(\theta_i) + n_i\sqrt{n_t^2 - n_i^2\sin^2(\theta_i)}}, \tag{46}$$

where $\perp$ and $\parallel$ denote the components perpendicular and parallel to the plane of incidence, respectively. Eqs. (45) and (46) are applicable to the cases with complex indices of refraction. As a consequence, the relative amplitudes are to be considered as complex values.

The reflection matrix is then (in Eqs. 3.16 of [42], replace S_1 by $r_\perp$ and S_2 by $r_\parallel$)

$$\mathbf{r}(\theta_i) = \frac{1}{2}\begin{pmatrix} r_\parallel^2 + r_\perp^2 & r_\parallel^2 - r_\perp^2 & 0 & 0 \\ r_\parallel^2 - r_\perp^2 & r_\parallel^2 + r_\perp^2 & 0 & 0 \\ 0 & 0 & 2\,\mathrm{Re}\{r_\perp r_\parallel^*\} & 2\,\mathrm{Im}\{r_\parallel r_\perp^*\} \\ 0 & 0 & 2\,\mathrm{Im}\{r_\perp r_\parallel^*\} & 2\,\mathrm{Re}\{r_\perp r_\parallel^*\} \end{pmatrix}, \tag{47}$$

where Re{} and Im{} denote the real and imaginary parts, respectively; the asterisk stands for the complex conjugate.

The transmission matrix $\mathbf{t}(\theta_i)$ is the following:

$$\mathbf{t}(\theta_i) = \frac{1}{2}\frac{n_t\cos(\theta_t)}{n_i\cos(\theta_i)}\begin{pmatrix} t_\parallel^2 + t_\perp^2 & t_\parallel^2 - r_\perp^2 & 0 & 0 \\ t_\parallel^2 - t_\perp^2 & t_\parallel^2 + r_\perp^2 & 0 & 0 \\ 0 & 0 & 2\,\mathrm{Re}\{t_\perp t_\parallel^*\} & 2\,\mathrm{Im}\{t_\parallel t_\perp^*\} \\ 0 & 0 & 2\,\mathrm{Im}\{t_\perp t_\parallel^*\} & 2\,\mathrm{Re}\{t_\perp t_\parallel^*\} \end{pmatrix}, \tag{48}$$

where the extra factor $n_t\cos(\theta_t)/n_i\cos(\theta_i)$ takes the following facts into account:

I the irradiance is proportional to the index of refraction (see [50], Eq. 1.53);

II the irradiance is proportional to the projected areas of the electromagnetic waves, which are in turn proportional to $\cos(\theta_i)$ for the incident wave and $\cos(\theta_t)$ for the transmitted wave, respectively.

7. Fourier series of the reflection and transmission matrices

The procedure by Deuzé et al. [45] has been employed to obtain the Fourier series of the reflection and transmission matrices. For the reflection matrix, the Fourier expansion of the scalar function h_r is needed:

$$h_r(\mu,\phi,\mu',\phi') = \sum_{k=0}^{K}(2-\delta_{0,k})h_r^k(\mu,\mu')\cos(k(\phi-\phi')), \tag{49}$$

where

$$h_r^k(\mu,\mu') = \frac{1}{2\pi}\int_0^{2\pi} h_r(\mu,\phi,\mu',\phi')\cos(k(\phi-\phi'))\,d\phi'. \tag{50}$$

Deuzé et al. [45] have used numerical integration procedures to evaluate Eq. (50). Alternatively, we use an analytical method. Substituting Eq. (29c) into Eq. (50), one has

$$\begin{aligned} h_r^k(\mu,\mu') &= A_r\exp(-a_r)\frac{1}{2\pi}\int_0^{2\pi}\exp(b_r\cos(k(\phi-\phi')))\cos(k(\phi-\phi'))\,d\phi', \\ &= A_r\exp(-a_r)I_k(b_r), \end{aligned} \tag{51}$$

where I_k is the modified Bessel functions of the first kind [51]. There are standard software packages available to numerically evaluate this special function [52]. Generally, the modified Bessel function of the first kind can be calculated via the recursion relation with decreasing k:

$$I_{k-1}(z) - I_{k+1}(z) = \frac{2k}{z}I_k(z), \tag{52}$$

where z is an arbitrary variable. It is preferable to use this procedure because it is more efficient and accurate than the numerical integration procedure.

The Fourier expansion of the matrix part $\mathbf{F}_r(\Theta)$ in $\mathbf{B}_r$ (Eq. (29a)) is

$$\begin{aligned} \mathbf{F}_r(\mu,\phi,\mu',\phi') = \sum_{l=0}^{L}(2-\delta_{0l})\{&\cos[l(\phi-\phi')]\mathbf{F}_{r,\cos}^l(\mu,\mu') \\ &+\sin[l(\phi-\phi')]\mathbf{F}_{r,\sin}^l(\mu,\mu')\}. \end{aligned} \tag{53}$$

To find $\mathbf{F}_{r,\cos}^l$ and $\mathbf{F}_{r,\sin}^l$, the effective scattering matrix is defined for convenience:

$$\begin{aligned} \mathbf{S}_{r,eff} &= (1-\cos(\Theta))^2\mathbf{r}((\pi-\Theta)/2) \\ &= \begin{pmatrix} a_1(\cos(\Theta)) & b_1(\cos(\Theta)) & 0 & 0 \\ b_1(\cos(\Theta)) & a_2(\cos(\Theta)) & 0 & 0 \\ 0 & 0 & a_3(\cos(\Theta)) & b_2(\cos(\Theta)) \\ 0 & 0 & -b_2(\cos(\Theta)) & a_4(\cos(\Theta)) \end{pmatrix}, \end{aligned} \tag{54}$$

where the matrix elements can be expanded in terms of the Wigner d functions d_{mn}^l [50,53]:

$$a_1 = \sum_{l=0}^{L}\beta_l d_{00}^l(\Theta), \tag{55a}$$

$$a_2 = \sum_{l=2}^{L}\{\alpha_l[d_{22}^l(\Theta) + d_{2,-2}^l(\Theta)] + \zeta_l[d_{22}^l(\Theta) - d_{2,-2}^l(\Theta)]\}, \tag{55b}$$

$$a_3 = \sum_{l=2}^{L}\{\zeta_l[d_{22}^l(\Theta) + d_{2,-2}^l(\Theta)] + \alpha_l[d_{22}^l(\Theta) - d_{2,-2}^l(\Theta)]\}, \tag{55c}$$

$$a_4 = \sum_{l=0}^{L}\delta_l d_{00}^l(\Theta), \tag{55d}$$

$$b_1 = \sum_{l=2}^{L}\gamma_l d_{20}^l(\Theta), \tag{55e}$$

$$b_2 = -\sum_{l=2}^{L}\varepsilon_l d_{20}^l(\Theta). \tag{55f}$$

The expansion coefficients are

$$\beta_l = \frac{2l+1}{2}\int_{-1}^{1} a_1(\cos(\Theta))d^l_{00}(\Theta)d\cos(\Theta), \tag{56a}$$

$$\alpha_l+\zeta_l = \frac{2l+1}{2}\int_{-1}^{1} \{[a_2(\cos(\Theta))+a_3(\cos(\Theta))]d^l_{2,2}(\Theta)d\cos(\Theta), \tag{56b}$$

$$\alpha_l-\zeta_l = \frac{2l+1}{2}\int_{-1}^{1} \{[a_2(\cos(\Theta))-a_3(\cos(\Theta))]d^l_{2,-2}(\Theta)d\cos(\Theta), \tag{56c}$$

$$\delta_l = \frac{2l+1}{2}\int_{-1}^{1} a_4(\cos(\Theta))d^l_{00}(\Theta)d\cos(\Theta), \tag{56d}$$

$$\gamma_l = \frac{2l+1}{2}\int_{-1}^{1} b_1(\cos(\Theta))d^l_{20}(\Theta)d\cos(\Theta), \tag{56e}$$

$$\varepsilon_l = -\frac{2l+1}{2}\int_{-1}^{1} b_2(\cos(\Theta))d^l_{20}(\Theta)d\cos(\Theta). \tag{56f}$$

Then the Fourier series of Eq. (29b) can be expressed as summations of these coefficients multiplying the Wigner d functions at different pairs of (μ,μ') [9,46,47,54].

Given h^k_r, $\mathbf{F}^l_{r,\cos}$, and $\mathbf{F}^l_{r,\sin}$, the Fourier series of the reflection matrix Eq. (29a) can then be found by the following equations [28,45]:

$$|\mu'|\mathbf{B}_r(\mu,\phi,\mu',\phi') = \sum_{m=0}^{M}(2-\delta_{0m})\{\cos[m(\phi-\phi')]|\mu'|\mathbf{B}^m_{r,\cos}(\mu,\mu') + \sin[m(\phi-\phi')]|\mu'|\mathbf{B}^m_{r,\sin}(\mu,\mu')\}, \tag{57}$$

where

$$|\mu'|\mathbf{B}^m_{r,\cos}(\mu,\mu') = h^m_r(\mu,\mu')\mathbf{F}^0_{r,\cos}(\mu,\mu') + \sum_{l=1}^{L}[h^{m+l}_r(\mu,\mu') + h^{|m-l|}_r(\mu,\mu')]\mathbf{F}^l_{r,\cos}(\mu,\mu'), \tag{58a}$$

$$|\mu'|\mathbf{B}^m_{r,\sin}(\mu,\mu') = -\sum_{l=1}^{L}[h^{m+l}_r(\mu,\mu')-h^{|m-l|}_r(\mu,\mu')]\mathbf{F}^l_{r,\sin}(\mu,\mu'). \tag{58b}$$

This procedure works well for the air-incident case. However, it does not work for the water-incident case because the Fresnel's reflection matrix changes abruptly around the critical angle $\theta_{i,c} = \arcsin(1/n_w) \approx 48.36^\circ$ (beyond which the total internal reflection happens), which prevents the polynomial expansions in Eq. (55f) from converging even for hundreds of terms. Figs. 2 and 3 show the effective scattering matrix elements in Eq. (54) for the air- and water-incident cases, respectively. Note that a_4 and b_2 are not shown because $a_4 = a_3$ and b_2 has values different from zero only for the case of internal reflection. The maximum order of expansion is $L = 36$ in both cases. The curves labeled "Exact" are calculated from Fresnel's law directly (after adjustments by the factor of $(1-\cos(\Theta))^2$). The curves labeled "Fit" are calculated with fitting parameters in Eq. (55a). It is readily observed that the air-incident matrix elements behave smoothly and the fitted curves overlap to the exact curves. The curves for the water-incident case, however, have sharp peaks/corners at $\Theta = 83.27^\circ$, which corresponds to $\theta_i = (\pi-\Theta)/2 = 48.36^\circ$. Attempting to reproduce these peaks, the polynomial expansion generates oscillations about the "exact" curves. Including a larger number of orders of scattering reduces, yet does not eliminate, the amplitude of these oscillations. Even for $L = 200$, the errors are still deemed unacceptable. Thus, we use direct numerical integration over $\phi = \phi-\phi'$ to find the Fourier components for the water-incident case:

$$|\mu'|\mathbf{B}^m_{r,\cos}(\mu,\mu') = \frac{1}{2\pi}\int_0^{2\pi} |\mu'|\mathbf{B}_r(\mu,\mu',\phi)\cos(m\phi)\,d\phi, \tag{59a}$$

$$|\mu'|\mathbf{B}^m_{r,\sin}(\mu,\mu') = \frac{1}{2\pi}\int_0^{2\pi} |\mu'|\mathbf{B}_r(\mu,\mu',\phi)\sin(m\phi)\,d\phi. \tag{59b}$$

The procedure to find the Fourier series of the transmission matrix is similar to the reflection matrix for the air-incident case outlined by equations from Eqs. (49) to (59). The Fourier components of the scalar function h_t are:

$$h^k_t(\mu,\mu') = A_t\exp(-a_t)I_k(b_t), \tag{60}$$

where A_t, a_t, and b_t are defined in Eq. (40a) for the air-incident case. Note that A_t, a_t, and b_t should be replaced by A'_t, a'_t, and b'_t in Eq. (42a) for the water-incident case. The effective scattering matrix for transmission is defined as

$$\mathbf{S}_{t,eff} = (n_w-\cos(\Theta))(n_w\cos(\Theta)-1)\mathbf{t}(\theta_i), \tag{61}$$

This matrix can be expanded in terms of the Wigner d functions as Eq. (55). Then the Fourier components $\mathbf{F}^l_{t,\cos}$ and $\mathbf{F}^l_{t,\sin}$ for $\mathbf{F}_t(\Theta)$ in Eqs. (40) and (42) can be found by the method outlined in [9,46,47,54]. Finally, the Fourier components $|\mu'|\mathbf{B}^m_{t,\cos}(\mu,\mu')$ and $|\mu'|\mathbf{B}^m_{t,\sin}(\mu,\mu')$ for the transmission matrix $|\mu'|\mathbf{B}_t$ are obtained using Eq. (58) provided that the subscript r is replaced by t.

If the dependence of the wind direction is introduced, i.e., the full Gram–Charlier expansion of Eq. (18) of Ref. [12] is used, it will be incorrect to write the Fourier expansions of the reflection and transmission matrices in the same way as Eq. (11) because these matrices depend on specific values of ϕ' and ϕ instead of $\phi-\phi'$. As a result, Eqs. (10) will not be correct because the Fourier expansion of the radiance field will also have sine components. Thus the whole system of equation will need to be revisited.

8. Validation

A Fortran 90 computer code was written to solve the VRT equation in the AOS. Basically, we have implemented the rough ocean boundary conditions into the previous version of our SOS code [9]. The exponential-linear approximation [41] is used to calculate the optical depth integration in Eqs. (12a) and (12b). The Gaussian quadrature formulas are used to evaluate the angular integrations in Eqs. (13) and (15). In the following we use N_a and N_o to denote the numbers of the Gaussian quadrature points for the atmosphere and ocean, respectively. Zhai et al. [9] presented an algorithm of implementing the flat ocean boundary condition in which $N_a = N_o$ is used. For the case of a rough surface, this is not feasible because of two reasons. First of all, the incident beam suffers from angular redistribution upon reflection and transmission.

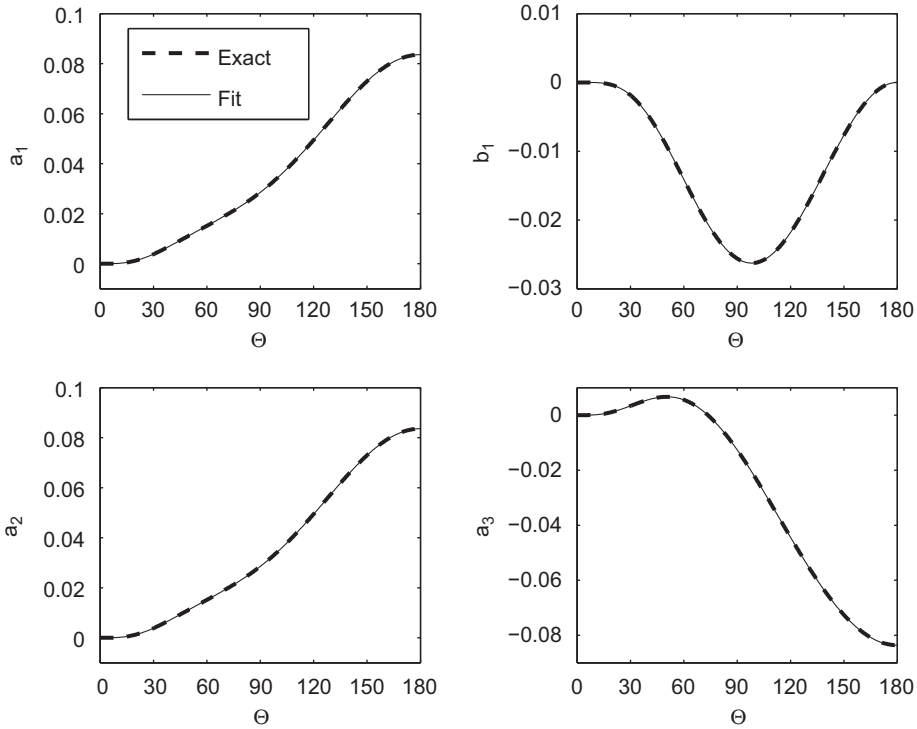

Fig. 2. The effective scattering matrix $\mathbf{S}_{r,eff}$ elements shown in Eq. (54) as a function of the scattering angle Θ for the air-incident case. The maximum order of expansion is $L=36$.

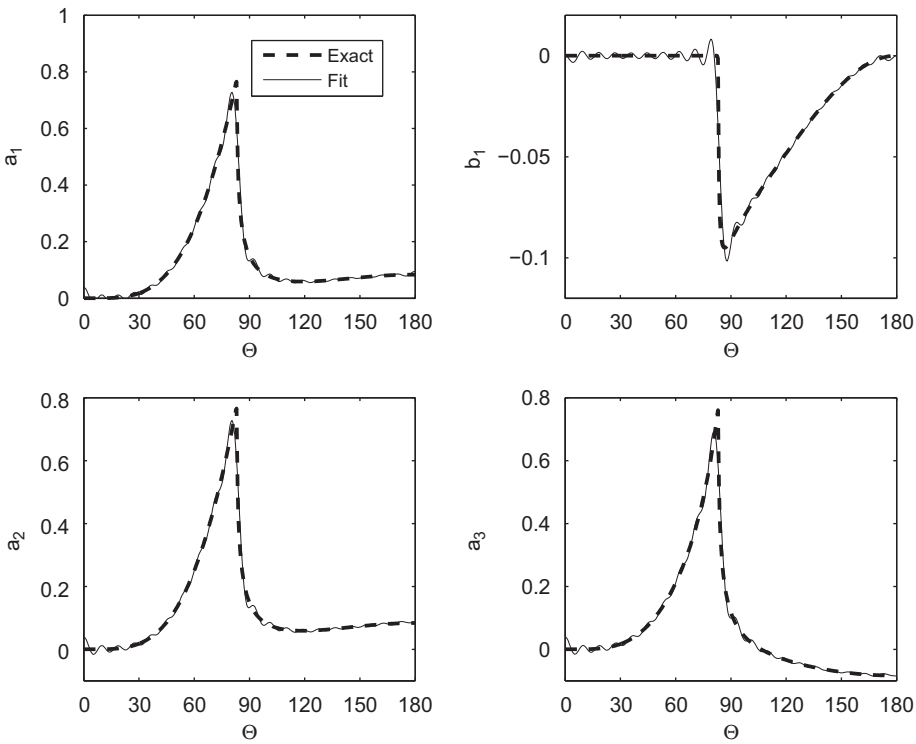

Fig. 3. The same as Fig. 2 except for the water-incident case. The maximum order of expansion is $L=36$.

Secondly, the angular distribution of the transmitted light (Eq. (34)) exhibits a delta function like peak, which is around the transmitted direction, as if the surface were smooth. Thus an interpolation scheme does not work well. In this work we use separate Gaussian quadrature points for atmosphere and ocean. The selection of the quadrature points and weights is the same as in [6].

To date, there is no benchmark data available to verify a VRT code in the AOS. Our strategy is then to verify different branches of our code with independent computer packages and related publications in the literature. For the simple case of an AOS with a flat interface, our code was found to compare well with Monte Carlo simulations [9]. For an AOS with a rough interface, the reflection matrix calculated by our subroutines agrees with the reflection matrix code by Mishchenko [40,55] with at least 5 significant digits (results not shown). For the transmission matrix, there is no published data to our knowledge. Therefore we used a radiative transfer code based on the doubling/adding method [22] to generate a dataset for comparison. The data is for an AOS in which the ocean is a conservative Rayleigh medium with an optical depth of 10. There is no lower boundary for the ocean. The wind speed is 7 m/s and the refractive index of ocean is 1.34. There is no atmosphere and the detector is just above the ocean surface. In this system, the transmission matrix will be tested because only the radiance transmitted from the ocean is detected. Fig. 4 shows the comparison between the SOS code and the doubling/adding method. The relative radiance difference shown in Fig. 4(d) between the two codes is defined as $100*(I_{SOS}-I_{DA})/I_{DA}\%$, where subscript DA stands for the doubling/adding method. θ (see x-axis) and ϕ (see legend in (d)) are the viewing polar and azimuthal angles, respectively. Note that the Stokes parameter U is zero for both $\phi=0^\circ$ and 180°. For this reason there are only three lines in Fig. 4(c). The solar incident angle is 60°. For both methods, the ocean Gaussian quadrature number is $N_o=60$. For the SOS method, the finite step for the optical depth integration in Eq. (12) is $\delta\tau=0.01$. The total number of scattering orders is 400 in the SOS method. It is observed that the maximum relative differences between the two codes are only around 0.1%. These highly accurate results show that the formulas and implementations are consistent and correct for both methods.

9. Applications and results

We perform two error analyses in this section. The first is to study errors introduced by neglecting the polarization in the radiative transfer calculation for a realistic AOS. The solar zenith angle is 60° and the

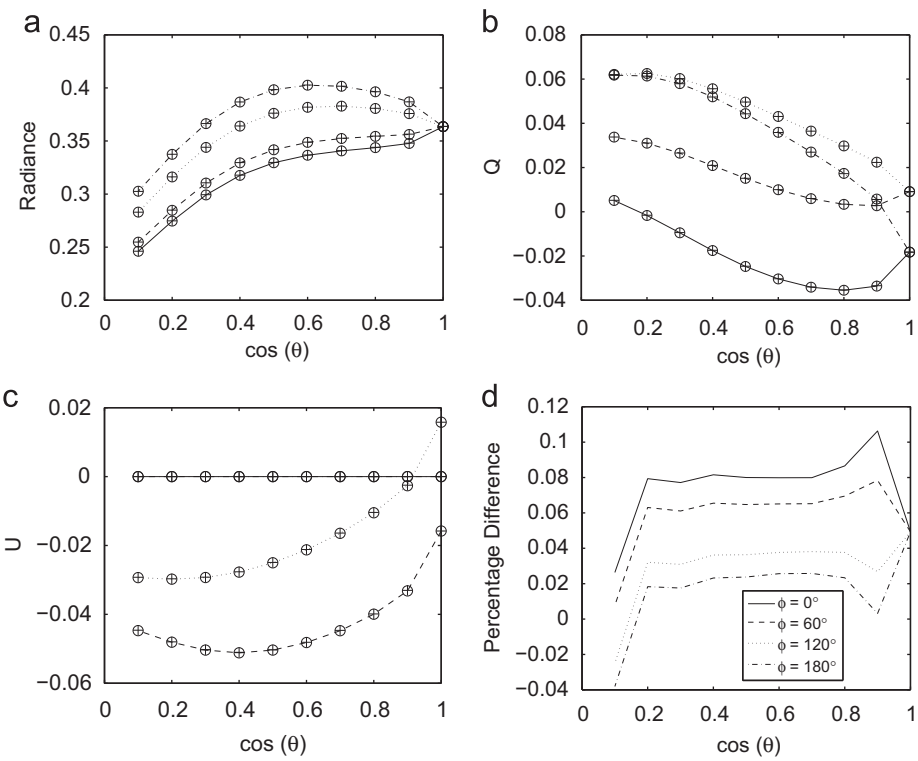

Fig. 4. Water leaving radiance and two other Stokes parameter elements Q and U. Circles show the results calculated by the doubling/adding method [22], while plus signs are calculated by the SOS method. Also shown in (d) is the percentage difference between the radiances calculated by the two methods. The ocean is a conservative Rayleigh medium with no lower boundary. The ocean optical depth is 10. The wind speed is 7 m/s and the refractive index of ocean is 1.34. There is no atmosphere and the detector is just above the ocean surface. θ (see x-axis) and φ (legend in (d) applies to all four subplots in Fig. 4) are the viewing polar and azimuthal angles, respectively. The solar incident angle is 60°.

wavelength is 555 nm. The atmosphere is a conservative Rayleigh medium with the optical thickness of 0.09375. The ocean surface is a rough surface whose slope distribution is given by the Cox–Munk model as in Eqs. (17) and (18). The ocean is Case 1 water as defined in [56]. There are three components in the ocean medium, which are pure seawater, phytoplankton pigments, and Colored Dissolved Organic Matter (CDOM). The IOPs of the ocean include the spectral absorption, scattering, extinction coefficients, and the scattering Mueller matrix. The total IOPs of the ocean water are modeled as the summation of the contributions of the three components. The total absorption coefficients a_t are

$$a_t = a_w + a_{CDOM} + a_{ph}, \tag{62}$$

where the subscripts w, $CDOM$, and ph stand for pure seawater, CDOM, and phytoplankton and their covariant particles, respectively. The water absorption coefficients a_w are taken from the tabulated experimental data by Pope and Fry [57]. The absorption by CDOM is estimated using the bio-optical model by Bricaud et al. [58]

$$a_{CDOM} = a_{CDOM}(440)\exp(-0.014(\lambda-440)), \tag{63}$$

where λ is the wavelength with a unit of nm and $a_{CDOM}(440) = 0.2[a_w(440) + a_{ph}(440)]$ [59]. The absorption coefficients of phytoplankton and their covariant particles are given by [59]:

$$a_{ph} = A_{ph}(\lambda)[Chl]^{E_p(\lambda)}, \tag{64}$$

where $[Chl]$ is the chlorophyll concentration in $\mathrm{mg\,m^{-3}}$. The tabulated coefficients A_{ph} and E_p were kindly provided by Bricaud. The scattering coefficient for the CDOM is treated as zero in the present study. Therefore, the scattering coefficients of the ocean water are

$$b_t = b_w + b_{ph}, \tag{65}$$

where b_w and b_{ph} are the scattering coefficients for pure seawater and phytoplankton and their covariant particles, respectively. The Einstein–Smoluchowski theory of fluctuation scattering provides b_w [16]:

$$b_w = 0.00193 \cdot (550/\lambda)^{4.32}. \tag{66}$$

The backscattering coefficient b_{bw} for the pure sea water is

$$b_{bw} = 1/2 \cdot b_w. \tag{67}$$

The bio-optical model for the particle scattering coefficients can be found in [60–62]. We adopt the most recent version in Huot et al. [60]:

$$b_{ph}(\lambda) = b_{ph}(660)\left(\frac{\lambda}{660}\right)^{\kappa}, \tag{68}$$

where

$$\begin{aligned} &\kappa = 0.5(\log_{10}[Chl]-0.3), && 0.02 < [Chl] < 2\,\mathrm{mg\,m^{-3}}, \\ &\kappa = 0, && [Chl] > 2\,\mathrm{mg\,m^{-3}}; \end{aligned} \tag{69}$$

and $b_{ph}(660)$ is the scattering coefficients at 660 nm:

$$b_{ph}(660) = 0.347[Chl]^{0.766}. \tag{70}$$

The backscatter fraction B_{bph} for phytoplankton and covarying particles is defined as the following ratio:

$$B_{bph} = b_{bph}/b_{ph}, \tag{71}$$

where b_{bph} is the backscattering coefficients. It is assumed that B_{bph} is spectrally neutral [60]:

$$B_{bph} = 0.002 + 0.01[0.5 - 0.25\log_{10}[Chl]]. \tag{72}$$

The total backscattering coefficient b_{bt} and backscatter fraction B_{bt} are

$$b_{bt} = b_{bw} + b_{bph}, \tag{73}$$

$$B_{bt} = b_{bt}/b_t. \tag{74}$$

The scattering function of the pure seawater is

$$F_w(\Theta) = 4\pi \cdot 0.06225(1 + 0.835\cos^2\Theta). \tag{75}$$

The scattering function used for the phytoplankton and their covariant particles is the Fournier–Forand (FF) scattering function, which is an analytical approximation to the scattering function of an ensemble of particles with a hyperbolic particle size-distribution [63,64]:

$$\begin{aligned} F_{FF}(\Theta) = {} & \frac{1}{(1-\delta)^2\delta^v}\{v(1-\delta)-(1-\delta^v) \\ & +[\delta(1-\delta^v)-v(1-\delta)]\sin^{-2}(\Theta/2)\} \\ & + \frac{1-\delta^v_{180^\circ}}{4(\delta_{180}-1)\delta^v_{180^\circ}}(3\cos^2\Theta-1), \end{aligned} \tag{76}$$

where

$$v = \frac{3-\gamma_{ph}}{2}, \quad \delta = \frac{4}{3(n_{ph}-1)^2}\sin^2\left(\frac{\Theta}{2}\right). \tag{77}$$

In these equations n_{ph} is the real index of refraction of the scatterers, γ_{ph} is the slope parameter of the hyperbolic size distribution, and δ_{180° is the value of δ at $\Theta = 180^\circ$. The FF scattering function is physically based on the Mie theory and can be generated conveniently from a given backscatter fraction B_{bph} by the algorithm in Mobley et al. [65]. For $B_{bph} = 0.0183$, the FF scattering function gives a fairly good approximation to the experimentally measured Petzold scattering function [66]. On the other hand, the detailed scattering function shape is not critical in the light field calculation if a correct backscatter fraction B_{bph} is provided [65]. These are the main motivations for adopting the FF scattering function in this study. The scheme in [65] is used for generating the FF scattering function given a value of B_{bph} in Eq. (72). For a given wavelength and $[Chl]$ value, the total scattering function for the ocean water is

$$F_t(\Theta) = \frac{b_w F_w(\Theta) + b_{ph} F_{FF}(\Theta)}{b_t}, \tag{78}$$

It is understood that b_w depends on the wavelength, b_{ph} depends on both the wavelength and chlorophyl concentration $[Chl]$, and F_{FF} depends on B_{bph}, which in turn depends on the wavelength and $[Chl]$.

The Mueller matrix of the ocean water is taken to be the averaged experimental measurement by Voss and Fry [67]. There are three nonzero matrix elements according to [67], which are $\overline{F}_{12} = \overline{F}_{21}$, $\overline{F}_{22}$, and $\overline{F}_{33} = \overline{F}_{44}$. The bar above each element shows the corresponding value is a reduced element, i.e., $\overline{F}_{ij} = F_{ij}/F_{11}$ where $F_{11} = F(\Theta)$ is the scattering function. Note that Voss and Fry [67] uses **S** instead of **F** to denote the Mueller matrix. **F** is adopted here to keep consistent with the formulas in this paper.

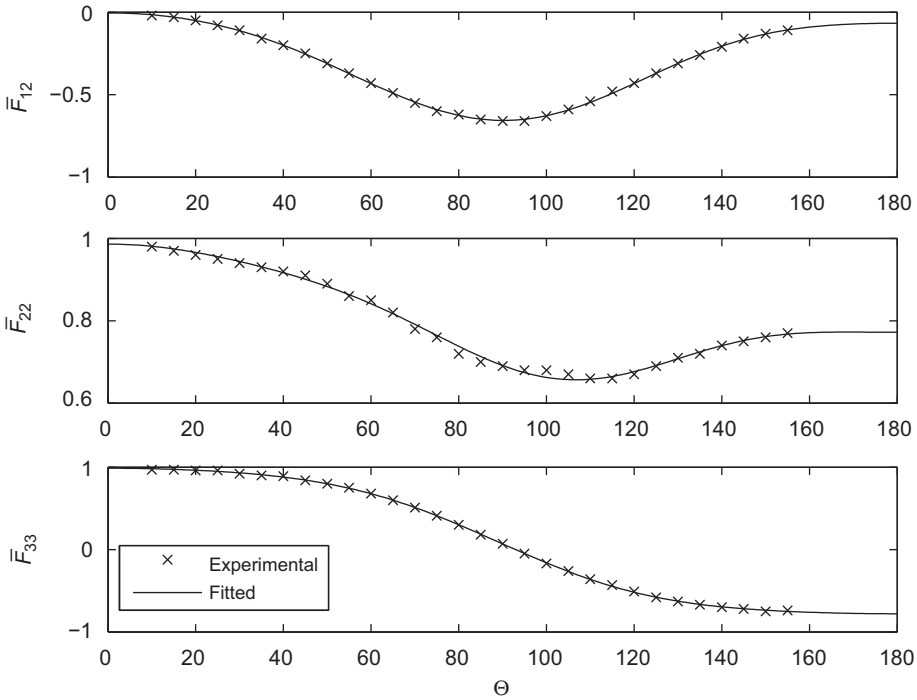

Fig. 5. The reduced Mueller matrix elements used in the model.

These elements were given in tabulated form starting from 10° to 155° with a 5° increment. To use these data in a numerical model, the nonzero Mueller matrix elements are modeled with the following expansion:

$$\overline{F}_{ij}(\Theta) = \sum_{l=0}^{6} c_{ij}^{l} P_l(\cos\Theta), \tag{79}$$

where P_l are the lth order Legendre Polynomials and c_{ij}^{l} are the expansion coefficients. The values of c_{ij}^{l} are found by the singular value decomposition method in solving the least squares fitting:

$$\varepsilon_{ij} = \sum_{k} \{\overline{F}_{ij,voss}(\Theta_k) - \overline{F}_{ij}(\Theta_k)\}^2 / \sigma_k^2, \tag{80}$$

where $\overline{F}_{ij,voss}(\Theta_k)$ are the experimental data presented by [67] and σ_k are the standard deviations. Fig. 5 shows the reduced Mueller matrix elements. The experimental results are given by the cross symbol and fitted results are given by solid lines. As pointed out by Voss and Fry, these matrix elements can never be modeled by the Mie theory for spherical particles because $\overline{F}_{22} \neq 1$. This is the major reason as to why this work does not use the Mie theory to calculate the scattering matrices.

The extinction coefficients are modeled as the summation of the absorption and scattering coefficients. The concentrations of phytoplankton is 0.3 mg/m^3. Several selected IOPs of the ocean water are reported in Table 1. The ocean optical depth is 10. The ocean bottom is set to be completely absorbing. Note that B_{bph}, B_{bt}, and ω are dimensionless.

Fig. 6 show the scalar radiance errors $100 * (I_{scalar} - I_{vector})/I_{vector}$ for the described AOS, where I_{scalar} and I_{vector} are the radiances calculated with the scalar and vector versions of our SOS code, respectively. The detector is at the top of the atmosphere (TOA). The Gaussian quadrature numbers $N_a = 36$ and $N_o = 72$ are used to make sure the calculations are accurate. The refractive index of the ocean water is taken as 1.34 in this case. Three wind speeds 0, 7, 14 m/s are used for simulations. For each polar plot, the zenith point is at the center, and the viewing polar angle of 90° is at the rim of the polar plot. The viewing azimuthal angles are shown around the plots. It is observed that the wind speed does change the scalar radiance errors, even though the effects are not very significant. Fig. 7 show the scalar radiance errors for two viewing azimuthal angles, $\phi = 80°$ and 180°, at which the scalar errors show a maximum and minimum, respectively. The changes of the scalar errors are several percents at the peak locations for the range of considered wind speeds. Simulations also show that the scalar errors for water leaving radiances (radiance from under the ocean interface) is small in comparison with the contribution from the Rayleigh atmosphere (results not shown). This is primarily because the water leaving light suffers more multiple scattering than the above water light. In an earlier work by Lacis et al. [19], the scalar errors were shown for a Rayleigh atmosphere bounded by a rough ocean surface (no ocean medium was considered).

Table 1
IOPs of Case 1 water for $[Chl] = 0.3\,\mathrm{mg/m^3}$ at 555 nm.

a_t (m^{-1})	b_t (m^{-1})	b_{bt} (m^{-1})	B_{bph}	B_{bt}	ω
6.48E−2	1.50E−1	2.16E−3	8.31E−3	1.44E−2	6.98E−1

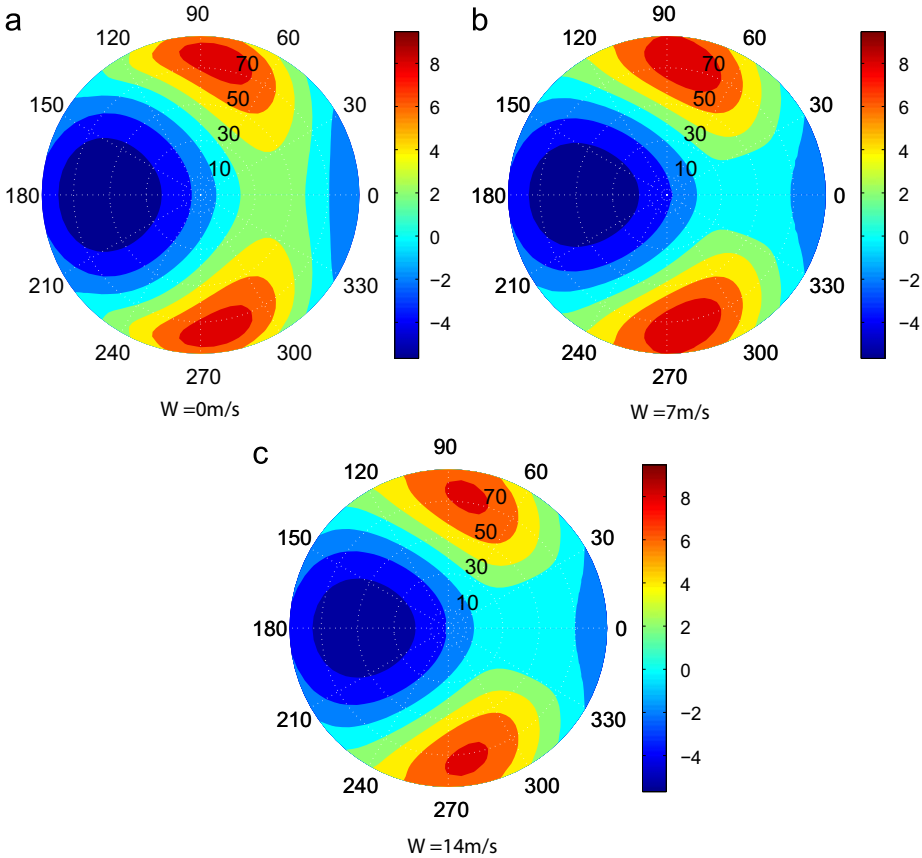

Fig. 6. Scalar radiance errors $100*(I_{scalar}\text{-}I_{vector})/I_{vector}$ for a coupled atmosphere and ocean system. Three cases are for the wind speeds 0, 7, 14 m/s, respectively. The solar zenith angle is 60°. The atmosphere is a conservative Rayleigh scattering medium with the optical thickness of 0.09375, which is for the wavelength of 555 nm. The ocean is based on the bio-optical model shown in the text with $[Chl]=0.3\,\mathrm{mg/m^3}$ at 555 nm. The ocean optical thickness is 10. There is no ocean bottom.

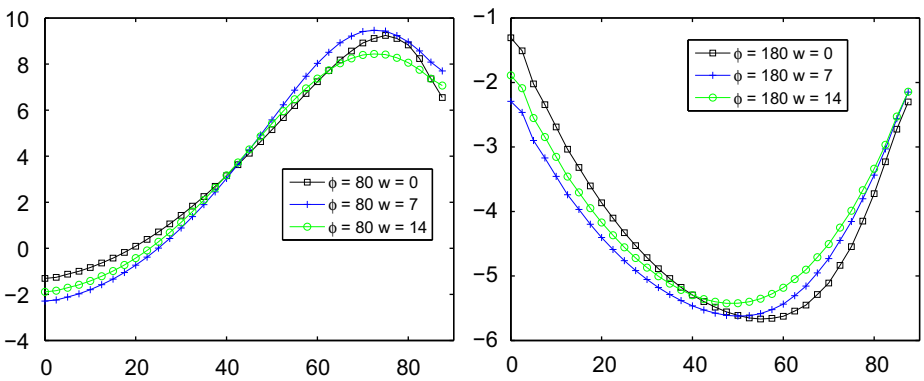

Fig. 7. Scalar radiance errors $100*(I_{scalar}\text{-}I_{vector})/I_{vector}$ as a function of viewing zenith angle θ for $\varphi=80°$ and 180°. The system is the same as in Fig. 6.

The results in [19] are similar to Fig. 6 because the small contribution of scalar errors from the water leaving radiances.

We also investigated the error introduced by ignoring the polarization of the transmitted radiance across the ocean interface. Generally, the ocean color remote sensing algorithms do take the polarization caused by atmospheric scattering into account; however, they still tend to ignore the polarization of the water leaving radiance [68]. This polarization originates not only from underwater light scattering, but also from transmission through the ocean surface. The latter polarization can be

as large as 30% for unpolarized incident light [21]. It is also perpendicular to the former polarization, which causes a reduction in the radiance of light emerging from the combined system of ocean surface and ocean water. In the following we explore the effects of ignoring the polarization of transmission through the ocean surface, i.e., by setting the ocean surface transmission matrices $\mathbf{B}_t$ and $\mathbf{B}_t'$ to zero except for their $(1,1)$ element. Fig. 8 shows the resulting relative change in water leaving radiances. The viewing geometries and scattering properties for the atmosphere and ocean body are the same as those used for Fig. 6. The results are now for observations just above the ocean surface instead of at the TOA. Errors as large as 20% are observed for $W=0$ m/s as one approaches the horizon in the azimuthal plane of $\phi=0^\circ$, but they remain smaller than 5% for $60^\circ<\phi<300^\circ$ and/or viewing angles less than 50°. Note that this distribution of errors is consistent with the distribution of polarized water leaving radiances which becomes largest in the $\phi=0^\circ$ plane (cf. Fig. 11 of Chowdhary et al. [23]), and with the increase towards large viewing angles of polarization induced by ocean surface transmission (cf. Fig. 5 of Kattawar and Adams [21]). Increasing the wind speed from $W=0$ to 14 m/s reduces the peak error and smoothes further out the whole error field. Fig. 8 suggests that an exact VRT model is desired to further reduce the uncertainties related to ocean color remote sensing.

Another important aspect of a computer code is the CPU time. For the SOS code presented in this paper, the CPU time mainly depends on the number of Gaussian points N_a and N_o, the maximum order of the Fourier expansion M, the optical depth of the atmosphere and ocean, the finite step $\delta\tau$ to do optical depth integration, and total order of scattering N. we designed one case to give readers some ideas about the computational speed of the SOS code. The atmosphere is chosen to be a conservative Rayleigh layer with the optical depth of 0.001. The purpose of this *thin* atmosphere is to minimize the CPU time contribution from the atmosphere so one can focus on the ocean. The ocean medium is a conservative Rayleigh layer with the optical depth of 1. The wind speed is set to 3 m/s even though this number would have no impact on the CPU time. The finite step for the optical depth integration is $\delta\tau=0.1$ for the ocean. The optical depth of the atmosphere is so small that it does not have to be further divided. The Gaussian quadrature numbers are $N_a=10$ and $N_o=20, 40, 60, 80, 100$, and 120. In this scenario the CPU Time per order of scattering N per

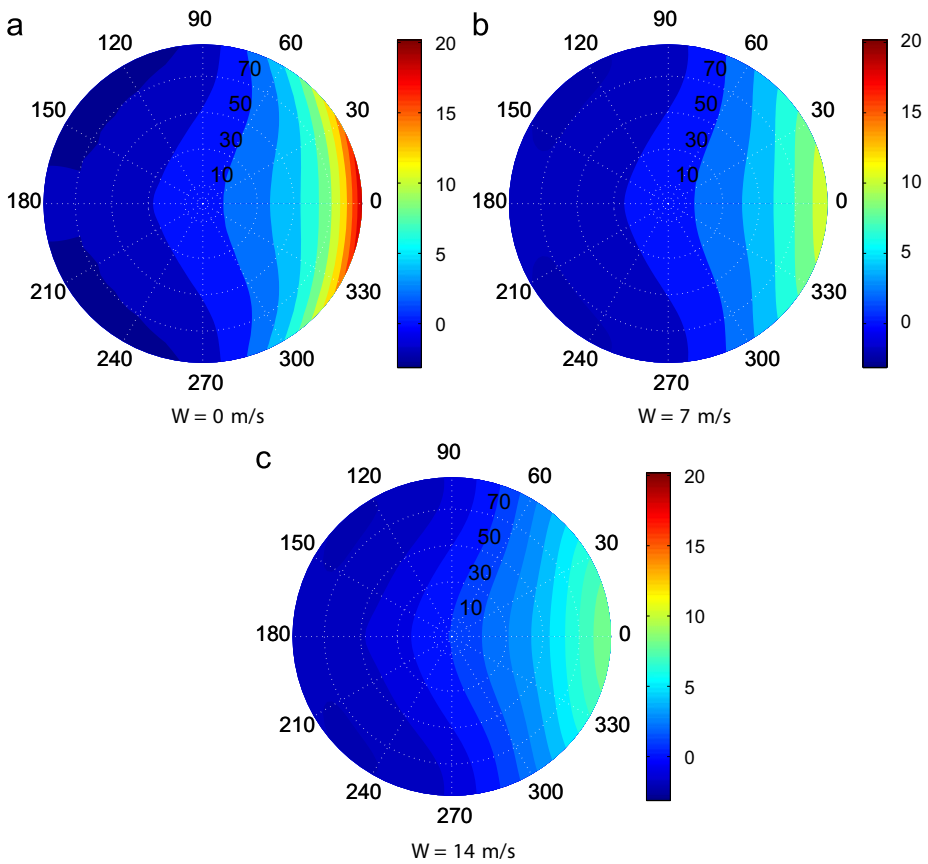

Fig. 8. Relative radiance errors $100*(I_{wlr,nTp}-I_{wlr,vector})/I_{wlr,vector}$ for a coupled atmosphere and ocean system, where the subscript *wlr* stands water leaving radiance; and *nTp* stands for the case ignoring the polarization of the transmitted radiances across the ocean interface. Other system parameters are the same as in Fig. 6.

order of Fourier expansion M can be well approximated by

$$\text{CPU Time}/N/M = 4.7079 \times 10^{-6} N_o^2 + 0.00020609 N_o + 0.0012333\,\text{s} \quad (81)$$

with the unit of seconds, with normal of residuals equal to 8.3082e-05s. The computer used to run the code is an I-Mac with a 2.8 Ghz Intel processor. The fortran compiler is GFORTRAN with the $-O3$ compile option. Note that $N = 10-40$ should be enough for most applications [9,31]. If a total order of scattering $N = 10$ and a Fourier order of $M = 3$ are used, the total CPU time will be 0.915 s with $N_o = 60$.

10. Summary

In this paper we present a VRT model for the AOS based on the SOS method. The wave slope distribution of the rough ocean surface is modeled as the Cox–Munk Gaussian distribution [11,12]. The reflection and transmission matrices have been derived based on the geometric optics approximation. Shadowing effects are considered by using the shadowing function. The four Stokes parameters can be obtained at arbitrary locations in the AOS. The Fourier series of the reflection and transmission matrices of a rough ocean surface are calculated by the methods of both Deuzé et al. [45] and direct integration. The SOS code is highly accurate with a maximum relative difference from the doubling/adding method [22] around 0.1% in a designed case study. We have performed two error analyses in the coupled atmosphere and ocean system. One is the scalar error in which the polarization of whole system is ignored. The other is the error introduced by ignoring the polarization of the light transmitted across the ocean interface. Both errors are found to be significant for the cases studied. Our next step consists of extending the comparison of Stokes parameters discussed in this work to include a variety of atmosphere–ocean systems, and of compiling a representative set of benchmark results. These results will benefit the ocean optics community in the validation of existing VRT codes and/or in the development of new VRT codes for coupled atmosphere–ocean systems.

Acknowledgments

This study is supported by the NASA Radiation Science program administrated Hal Maring and the Biogeochemistry program administrated by Paula Bontempi. We would like to thank A. Bricaud for the absorption coefficient data. We would also like to appreciate valuable discussions with Bing Lin about the shadowing effects for a rough surface. And we appreciate two anonymous reviewers for their thoughtful and helpful comments

References

[1] Chandrasekhar S. Radiative transfer. New York: Dover; 1960.
[2] Preisendorfer RW. Radiative transfer on discrete spaces. Oxford: Pergamon Press; 1965.
[3] Mishchenko MI, Travis LD, Lacis AA. Multiple scattering of light by particles. New York: Cambridge University Press; 2006.
[4] Stephens GL. Remote sensing of the lower atmosphere: an introduction. New York: Oxford University Press; 1994.
[5] Liou KN. An introduction to atmospheric radiation, 2nd ed.. San Diego: Academic; 2002.
[6] Jin Z, Stamnes K. Radiative transfer in nonuniformly refracting layered media: atmosphere–ocean system. Appl Opt 1994;33: 431–42.
[7] Bulgarelli B, Kisselev VB, Roberti L. Radiative transfer in the atmosphere–ocean system: the finite-element method. Appl Opt 1999;38:1530–42 〈http://www.opticsinfobase.org/ao/abstract.cfm?URI=ao-38-9-1530〉.
[8] Chami M, Santer R, Dilligeard E. Radiative transfer model for the computation of radiance and polarization in an ocean–atmosphere system: polarization properties of suspended matter for remote sensing. Appl Opt 2001;40:2398–416 〈http://www.opticsinfobase.org/abstract.cfm?URI=ao-40-15-2398〉.
[9] Zhai P, Hu Y, Trepte CR, Lucker PL. A vector radiative transfer model for coupled atmosphere and ocean systems based on successive order of scattering method. Opt Express 2009;17:2057–79.
[10] Sommersten ER, Lotsberg JK, Stamnes K, Stamnes JJ. Discrete ordinate and Monte Carlo simulations for polarized radiative transfer in a coupled system consisting of two media with different refractive indices. J Quant Spectrosc Radiat Transf. in press, DOI: 10.1016/j.jqsrt.2009.10.021. 〈http://www.sciencedirect.com/science/article/B6TVR-4XKXXWR-1/2/418e1072225240ef2ec5a31e16447d7a〉.
[11] Cox C, Munk W. Statistics of sea surface derived from sun glitter. J Mar Res 1954;13:198–227.
[12] Cox C, Munk W. Measurement of the roughness of the sea surface from photographs of the sun Os glitter. J Opt Soc Am 1954;44:838–50 〈http://www.opticsinfobase.org/josa/abstract.cfm?URI=josa-44-11-838〉.
[13] Nakajima T, Tanaka M. Effect of wind-generated waves on the transfer of solar radiation in the atmosphere–ocean system. J Quant Spectrosc Radiat Transfer 1983;29:521–37.
[14] Fischer J, Grassl H. Radiative transfer in an atmosphere–ocean system: an azimuthally dependent matrix operator approach. Appl Opt 1984;23:1032–9.
[15] Mobley CD, Gentili B, Gordon HR, Jin Z, Kattawar GW, Morel A, et al. Comparison of numerical models for computing underwater light fields. Appl Opt 1993;32:7484–504.
[16] Mobley CD. Light and water: radiative transfer in natural waters. San Diego: Academic; 1994.
[17] Jin Z, Charlock TP, Rutledge K, Stamnes K, Wang Y. Analytical solution of radiative transfer in the coupled atmosphere–ocean system with a rough surface. Appl Opt 2006;45:7443–55.
[18] Mishchenko MI, Lacis AA, Travis LD. Errors induced by the neglect of polarization in radiance calculations for Rayleigh-scattering atmospheres. J Quant Spectrosc Radiat Transfer 1994;51:491–510.
[19] Lacis AA, Chowdhary J, Mishchenko MI, Cairns B. Modeling errors in diffuse-sky radiation: vector vs. scalar treatment. Geophys Res Lett 1998;25:135–8.
[20] Masuda K, Takashima T. Computational accuracy of radiation emerging from the ocean surface in the model atmosphere–ocean system. Pap Met Geophys 1986;37:1–13.
[21] Kattawar GW, Adams CN. Stokes vector calculations of the submarine light field in an atmosphere–ocean with scattering according to a Rayleigh phase matrix: effect of interface refractive index on radiance and polarization. Limnol Oceanogr 1989;34: 1453–72.
[22] Chowdhary J. Multiple scattering of polarized light in atmosphere–ocean systems. PhD thesis, Columbia University, New York; 1999.
[23] Chowdhary J, Cairns B, Travis LD. Contribution of water-leaving radiances to multiangle multispectral polarimetric observations over the open ocean: bio-optical model results for case 1 waters. Appl Opt 2006;45:5542–67 〈http://www.opticsinfobase.org/abstract.cfm?URI=ao-45-22-5542〉.
[24] Zhai P, Kattawar GW, Yang P. Impulse response solution to the three-dimensional vector radiative transfer equation in atmosphere–ocean systems. I. Monte Carlo method. Appl Opt 2008;47:1037–47 〈http://www.opticsinfobase.org/abstract.cfm?URI=ao-47-8-1037〉.
[25] Spurr RJD. LIDORT and VLIDORT linearized pseudo-spherical scalar and vector discrete ordinate radiative transfer models for use in remote sensing retrieval problems. In: Kokhanovsky AA, editor. Light scattering reviews, vol. 3. Berlin: Springer; 2008. p. 229–71.
[26] Hammad A, Chapman S. The primary and secondary scattering of sun light in a plane-stratified atmosphere of uniform composition. Philos Mag 1939;28:99–110.

[27] Lenoble J, editor. Radiative transfer in scattering and absorbing atmospheres: standard computational procedures. A. Deepak Publishing; 1985.
[28] Lenoble J, Herman M, Deuzé JL, Lafrance B, Santer R, Tanré D. A successive order of scattering code for solving the vector equation of transfer in the earth Os atmosphere with aerosols. J Quant Spectrosc Radiat Transfer 2007;107:479–507.
[29] Myneni RB, Asrar G, Kanemasu ET. Light scattering in plant canopies: the method of successive orders of scattering approximations (SOSA). Agric For Meteorol 1987;39:1–12.
[30] Lenoble J. Atmospheric radiative transfer. A. Deepak Publishing; 1993.
[31] Min Q, Duan M. A successive order of scattering model for solving vector radiative transfer in the atmosphere. J Quant Spectrosc Radiat Transfer 2004;87:243–59.
[32] Duan M, Min Q. A semi-analytic technique to speed up successive order of scattering model for optically thick media. J Quant Spectrosc Radiat Transfer 2005;95:21–32.
[33] Greenwald T, Bennartz R, O'Dell C, Heidinger A. Fast computation of microwave radiances for data assimilation using the 'successive order of scattering'' method. J Appl Meteorol 2005;44:960–6.
[34] Heidinger AK, O'Dell C, Bennartz R, Greenwald T. The successive-order-of-interaction radiative transfer model. part I: model development. J Appl Meteorol Climatol 2005;45:1388–402.
[35] Kotchenova SY, Vermote EF, Matarrese R, Klemm Jr FJ. Validation of a vector version of the 6S radiative transfer code for atmospheric correction of satellite data. Part I: path radiance. Appl Opt 2006;45:6762–74 〈http://www.opticsinfobase.org/abstract.cfm?URI=ao-45-26-6762〉.
[36] Kotchenova SY, Vermote EF. Validation of a vector version of the 6S radiative transfer code for atmospheric correction of satellite data. Part II. Homogeneous Lambertian and anisotropic surfaces. Appl Opt 2007;46:4455–64 〈http://www.opticsinfobase.org/abstract.cfm?URI=ao-46-20-4455〉.
[37] Suzuki T, Nakajima T, Tanaka M. Scaling algorithms for the calculation of solar radiative fluxes. J Quant Spectrosc Radiat Transfer 2007;107:458–69.
[38] Smith BG. Geometrical shadowing of a random rough surface. IEEE Trans Ant Prop 1967;15:668–71.
[39] Sancer MI. Shadow-corrected electromagnetic scattering from a randomly rough surface. IEEE Trans Ant Prop 1969;17:577–85.
[40] Mishchenko MI, Travis LD. Satellite retrieval of aerosol properties over the ocean using polarization as well as intensity of reflected sunlight. J Geophys Res 1997;102:16989–7013.
[41] Kylling A, Stamnes K. Efficient yet accurate solution of the linear transport equation in the presence of internal sources: the exponential-linear-in depth approximation. J Comput Phys 1992;102:265–76.
[42] Bohren CF, Huffman DR. Absorption and scattering of light by small particles. New York: Wiley; 1983.
[43] Hu Y, Winker D, Yang P, Baum B, Poole L, Vann L. Identification of cloud phase from PICASSO-CENA lidar depolarization: a multiple scattering sensitivity study. J Quant Spectrosc Radiat Transfer 2001;70:569–79.
[44] Van der Mee CVM, Hovenier JW. Expansion coefficients in polarized light transfer. Astron Astrophys 1990;228:559–68.
[45] Deuzé JL, Herman M, Santer R. Fourier series expansion of the transfer equation in the atmosphere–ocean system. J Quant Spectrosc Radiat Transfer 1989;41:483–94.
[46] Siewert CE. On the phase matrix basic to the scattering of polarized light. Astron Astrophys 1982;109:195–200.
[47] Hovenier JW, van der Mee CVM. Fundamental relationships relevant to the transfer of polarized light in a scattering atmosphere. Astron Astrophys 1983;128:1–16.
[48] Gautsch W. Error function and fresnel integrals. In: Abramowitz M, Stegun IA, editors. Handbook of mathematical functions with formulas, graphs, and mathematics tables, vol. 55. Washington: National Bureau of Standards; Tenth Printing 1972; 1964. p. 295–329.
[49] Jackson JD. Classical electrodynamics, 3rd ed.. New York: Wiley; 1998.
[50] Mishchenko MI, Travis LD, Lacis AA. Scattering absorption and emission of light by small particles. Cambridge: Cambridge University Press; 2002.
[51] Olver FWJ. Bessel functions of integer order. In: Abramowitz M, Stegun IA, editors. Handbook of mathematical functions with formulas graphs and mathematics tables, vol. 55. Washington: National Bureau of Standards; Tenth Printing 1972; 1964. p. 374–8.
[52] Cody WJ. Algorithm 715; SPECFUNa portable FORTRAN package of special function routines and test drivers. ACM Trans Math Software (TOMS) 1993;19:22–30.
[53] Wigner EP. Group theory and its application to the quantum mechanics of atomic spectra. New York: Academic Press; 1959.
[54] Kuščer I, Ribarič M. Matrix formalism in the theory of diffusion of light. Opt Acta 1959;6:42–51.
[55] Mishchenko MI, Zakharova NT. FORTRAN codes for the computation of the bidirectional reflection function for flat particulate layers and rough surfaces. Page updated: 2009-04-05, URL (〈http://www.giss.nasa.gov/staff/mmishchenko/brf/〉) (visited 2009-09-02).
[56] Morel A, Prieur L. Analysis of variations in ocean color. Limnol Oceanogr 1977;22:709–22.
[57] Pope RM, Fry ES. Absorption spectrum (380–700 nm) of pure water II integrating measurements. Appl Opt 1997;33:8710–23.
[58] Bricaud A, Morel A, Prieur L. Absorption by dissolved organic matter of the sea (yellow substance) in the UV and visible domains. Limnol Oceanogr 1981;26:43–53.
[59] Bricaud A, Morel A, Babin M, Allali K, Claustre H. Variations of light absorption by suspended particles with chlorophyll a concentration in oceanic (case 1) waters: analysis and implications for bio-optical models. J Geophys Res 1998;103:31033–44.
[60] Huot Y, Morel A, Twardowski MS, Stramski D, Reynolds RA. Particle optical backscattering along a chlorophyll gradient in the upper layer of the eastern South Pacific Ocean. Biogeosciences 2008;5:495–507.
[61] Loisel H, Morel A. Light scattering and chlorophyll concentration in case 1 waters: a reexamination. Limnol Oceanogr 1998;43:847–58.
[62] Morel A, Maritorena S. Bio-optical properties of oceanic waters: a reappraisal. J Geoph Res 2001;106:7163–80.
[63] Fourier G, Forand JL. Analytic phase function for ocean water. In: Jaffe JS, editor. Ocean optics XII. Proceedings of the SPIE, vol. 2258; 1994. p. 194–201.
[64] Fournier G, Jonasz M. Computer-based underwater imaging analysis. In: Gilbert G, editor. Airborne and in-water underwater imaging. Proceedings of the SPIE, vol. 3761; 1999. p. 62–77.
[65] Mobley CD, Sundman LK, Boss E. Phase function effects on oceanic light fields. Appl Opt 2002;41:1035–50.
[66] Petzold TJ. Volume scattering functions for selected ocean waters Scripps Institution of Oceanography. 1977.
[67] Voss KJ, Fry ES. Measurement of the Mueller matrix for ocean water. Appl Opt 1984;23:4427–39.
[68] Wang M. Aerosol polarizing effects on atmospheric correction and aerosol retrievals in ocean color remote sensing. Appl Opt 2006;45:8951–63.